**Short title:** Chlamydomonas ribosomes and cell cycle under ion stress

**Correspondence:**

Tobias Wunder

Plant Biochemistry and Physiology

LMU Munich

Großhaderner Str. 2-4, 82152 Planegg-Martinsried, Germany

Email: tobias.wunder@lmu.de

**Conserved and Lineage-Specific Roles of KEA-Mediated Ion Homeostasis in *Chlamydomonas***

Tobias Wunder[*+a], Leon Eulitz[a], Luis Kramer[a], Zahin Mohd Ali[b], Matthias Ostermeier[c], Charlott Leu[d], Beata Szulc[a], Lorenz J. Holzner[a], Jonas Fechter[a], Francesco Padovani[e], Benjamin Brandt[a], Philipp Girr[f], Jing Tsong Teh[c], Susanne Mühlbauer[a], Clara Sotos[g], Max Angstenberger[h], Luke C. M. Mackinder[f], Kurt M. Schmoller[e], Joachim O. Rädler[d], Jörg Nickelsen[c], Jan de Vries[b], Hans-Henning Kunz[+a]

[a] Plant Biochemistry and Physiology, LMU München, Großhaderner Straße 2-4, 82152, Martinsried-Planegg, Germany.

[b] Institute of Microbiology and Genetics, Göttingen Center for Molecular Biosciences (GZMB), Campus Institute Data Science (CIDAS), Department of Applied Bioinformatics, University of Göttingen, Goldschmidtstr. 1, 37077 Göttingen, Germany

[c] Molecular Plant Science, LMU Munich, Großhaderner Straße 2-4, 82152 Planegg-Martinsried, Germany.

[d] Faculty of Physics and Center for NanoScience, Ludwig-Maximilian-University, Geschwister-Scholl-Platz 1, D-80539 Munich, Germany

[e] Institute of Functional Epigenetics, Molecular Targets and Therapeutics Center, Helmholtz Zentrum Muenchen, 85764 Neuherberg, Germany

[f] Centre for Novel Agricultural Products (CNAP), Department of Biology, University of York, Heslington, York YO10 5DD, UK.

[g] Institute for Integrative Biology of the Cell (I2BC), Université Paris-Saclay, CEA, CNRS, 91198 Gif-sur-Yvette cedex, France.

[h] Institute of Molecular Biosciences, Goethe University Frankfurt, 60438 Frankfurt, Germany

*Corresponding author: Tobias Wunder, tobias.wunder@lmu.de

[+]Senior authors: Tobias Wunder, tobias.wunder@lmu.de, Hans-Henning Kunz, kunz@lmu.de

**Keywords: photosynthesis, ion balance, rRNA processing, cell cycle, microalgae, chloroplast**

**One-sentence summary**

Disruption of KEA-mediated chloroplast ion homeostasis in *Chlamydomonas reinhardtii* reveals conserved and lineage-specific control of plastid rRNA processing and cell cycle progression.

**Footnotes:**

**Author Contributions**

T.W. and H.-H.K. conceived research idea and wrote the manuscript. T.W. cloned constructs, isolated algal and plant mutants, performed most experiments, analyzed data, and designed the figures. L.E. performed single-cell imaging, analyzed image data, designed figures, and wrote sections. L.J.H. conducted TXRF and analyzed elemental data. C.S. generated plant mutants and helped with element analysis. L.K. and B.S. performed and assisted in RNA and growth experiments. J.F. carried out RNA-blots. M.A. isolated algal mutants. F.P. and K.M.S. supported analysis of single-cell imaging data. M.O. performed transmission electron microscopy. B.B. assisted with RNA-seq data analysis and visualization. P.G. and L.C.M.M. recombineered plasmids. Z.M.A. and J.dV. performed cross-species gene network analyses. C.L. and J.O.R. designed and fabricated hydrogel flow-cell chips. S.M. provided illustration. J.T.T. and J.N. designed and carried out initial CRISPR/Cas9. All authors assisted in editing the manuscript.

## Abstract

In *Arabidopsis thaliana*, seamless plastid gene expression and development depend on finely balanced ion homeostasis across the inner envelope (IE) membrane, maintained by the $K^+/H^+$ antiporters AtKEA1/2. To assess whether these functions are retained across mono- and polyplastidic representatives of the green lineage, we studied CrKEA1, the sole IE KEA homolog in the unicellular alga *Chlamydomonas reinhardtii*. Using CRISPR/Cas9, we generated a *kea1* knockout mutant that exhibits impaired photoautotrophic growth, chloroplast deformation, and photoinhibition. Transcriptomics revealed strong induction of ribosome biogenesis genes and reduced abundance of transcripts associated with cell and plastid division. Further RNA analyses confirmed defects in stromal rRNA maturation of *kea1*, paralleling observations from Arabidopsis *kea1kea2* mutants. Expression of *CrKEA1* in Arabidopsis rescued growth and rRNA maturation in *kea1kea2*, demonstrating functional continuity after the ancient divergence between the two lineages. Cross-species transcriptomic comparisons further revealed that IE *KEA* loss elicits both shared and species-specific transcriptional responses: *PhANG* repression was conserved between algae and plants, whereas activation of the chloroplast unfolded protein response (cpUPR) and reduced expression of genes tied to cell-cycle and plastid fission occurred only in Chlamydomonas. Single-cell time-lapse imaging confirmed that *kea1* exhibits an increased frequency of aberrant cytokinesis, unequal division, and division failure. Our findings demonstrate that while IE KEA transporters fulfill conserved roles in maintaining the conditions for plastid gene expression, their integration into broader cellular networks has diverged between unicellular chlorophytes and embryophytes (land plants). This underscores a lineage-dependent tuning of plastid-nucleus communication shaped by organismal complexity and plastid number.

## Introduction

A balanced ionic milieu is essential for plastid biogenesis and function (Kunz et al., 2024). In Arabidopsis (*Arabidopsis thaliana)*, disruption of the inner envelope (IE) $K^+/H^+$ antiporters KEA1 and KEA2 produces a virescent phenotype i.e., pale young leaves that eventually develop into green photosynthesizing tissue (Kunz et al., 2014). Subsequent work revealed that the essential role of KEA1/2 in plastid integrity and photosynthetic performance is linked to plastid gene expression and rRNA maturation (DeTar et al., 2021). These findings demonstrate a strong connection between organellar ion homeostasis and chloroplast biogenesis.

Dissecting this link mechanistically in plant cells is complicated due to their multicellular organization and polyplastidy: Plants typically harbor cells with dozens of plastids displaying heterogeneous behavior depending on tissue context and developmental stage (Knoblauch et al., 2024; Renna et al., 2025). This cellular heterogeneity makes it challenging to distinguish direct, plastid-autonomous consequences of ion imbalance from secondary effects at the tissue or organismal level.

Interestingly, many unicellular algae maintain a single plastid per cell. de Vries and Gould, 2018 described the evolutionary framework of the "monoplastidic bottleneck", which posits that the ancestor of all Archaeplastida (Figure 1A) passed through a stage where plastid and host cell division were strictly synchronized. The unicellular green algae Chlamydomonas (*Chlamydomonas reinhardtii*), with its single cup-shaped chloroplast, represents a bona fide example of this ancestral state. In contrast, land plants such as Arabidopsis, have since evolved polyplastidy and decoupled plastid division from the nuclear cycle. Thus, Chlamydomonas is an ideal model to study the direct relation between plastid physiology, cell growth, and division, as each cell depends on a single plastid for both metabolism and successful cytokinesis.

Despite around a billion years of divergence between chlorophyte algae and streptophyte plants (Figure 1A), IE KEA transporters are conserved across the green lineage, and orthologs are present in green algae (Kunz et al., 2024). This conservation raises the question of whether KEA proteins maintain mechanistic similarity or whether their roles have been rewired in line with lineage-specific cellular contexts.

In this study, we employ Chlamydomonas for an initial investigation into how KEA-mediated ion transport across plastid envelope membranes influences the organelle's function, cell physiology, and cell cycle in a unicellular, monoplastidic organism. By combining mutant analyses, transcriptome comparisons with Arabidopsis (DeTar et al., 2021), and cross-species complementation, we show that KEA function is a prerequisite for maintaining the integrity of ribosome biogenesis. Leveraging the complementary strengths of a multicellular polyplastidic plant and a unicellular monoplastidic alga (Gutman and Niyogi, 2004), we provide evidence that KEA's importance for plastid gene expression is deeply conserved, while its cellular consequences are shaped by lineage-specific developmental context.

73 **Results**

74 *Generation of CrKEA1 knock-out and complementation lines for subcellular localization studies*
75 *of CrKEA1*

76 *KEA* genes are conserved from green algae to angiosperms (Chanroj et al., 2012). Through
77 amino acid sequence homology analysis, we identified Cre04.g220200 (*CrKEA1*) in
78 Chlamydomonas as the only homolog of inner envelope (IE) $K^+/H^+$ exchangers AtKEA1/2 from
79 Arabidopsis (see alignment, Supplemental Figure S1). The conserved monovalent cation/proton
80 antiporter 2 (CPA2) domain and the regulatory $K^+$ transport and NAD-binding (KTN) domain
81 share 56% sequence identity and 71% similarity between plant and algae KEA1. In contrast, the
82 extended N-terminal region (~500 amino acids) — a characteristic feature of all IE KEAs that
83 includes a coiled-coil domain embedded within a highly disordered segment (Chanroj et al., 2012;
84 Bölter et al., 2020) — is far less conserved, showing only 13% identity and 29% similarity.

85 To investigate CrKEA1 function in Chlamydomonas, we initially generated a CrKEA1
86 antibody (Supplemental Figure S2, A-C) with a detection sensitivity against its antigen
87 (CrKEA1_aa94-337) in the picogram range (Supplemental Figure S2D). We attempted to utilize
88 mutant strain LMJ.RY0402.187220, which at the time was the only CLiP insertion line in the
89 *CrKEA1* locus (Li et al., 2016). However, protein expression in wild-type (WT) cells and
90 LMJ.RY0402.187220 was clearly detectable at an apparent size of ~120 kDa (calculated size 108
91 kDa for full length size, without estimated chloroplast targeting peptide, cTP, ~101 kDa),
92 confirming functionality of the CrKEA1 antibody with Chlamydomonas protein extracts but also
93 that the CLiP line had not lost CrKEA1 (Supplemental Figure S2E). We therefore turned towards
94 an established CRISPR/Cas9 protocol (Kelterborn et al., 2022) to generate *CrKEA1* knock-out
95 strains ourselves. We successfully isolated a *kea1* mutant with a stop codon insertion in exon 19
96 (Figure 1B), which was confirmed by PCR screening and Sanger sequencing (Supplemental Figure
97 S3, A-D; Supplemental Table S1). Immunoblotting further verified the loss of full-length CrKEA1
98 (Figure 1C; Supplemental Figure S3E). Lastly, we sequenced the genome of *kea1*, which allowed
99 us to annotate the entire insertion site (Supplemental Figure S3F, Figure S4) and to verify the
100 absence of additional CRISPR/Cas9-mediated insertions in this background.

101 To analyze the subcellular localization of CrKEA1, we generated several complementation
102 lines by transforming *kea1* with *CrKEA1* fused to a *YFP* at the C-terminus under the control of its
103 native promoter. Immunoblotting with the CrKEA1 antibody confirmed CrKEA1-YFP expression,

104 detecting a band at ~140 kDa that migrated ~30 kDa larger compared to the endogenous signal
105 (Figure 1C; Supplemental Figure S5A) — consistent with the added YFP tag (calculated 138 kDa
106 full length, 132 kDa without cTP). Subsequently, we performed fluorescence microscopy and
107 found the YFP fluorescence signal to emerge from the membrane that surrounds the chlorophyll
108 autofluorescence. This confirms that CrKEA1, consistent with its plant homologs, resides in the
109 plastid envelope membrane (Figure 1D; Supplemental Figure S6).

110 *Hampered growth upon loss of CrKEA1 in kea1 strains*

111 Chlamydomonas can grow hetero- and mixotrophically on acetate-supplemented TAP
112 medium or autotrophically in HSM medium, relying entirely on $CO_2$ fixation via RuBisCO (Sager
113 and Zalokar, 1958; Harris et al., 2009; Grossman et al., 2010; Lauersen et al., 2016). To assess the
114 impact of CrKEA1 loss, we tested our strains under different growth conditions at 23°C. Initially,
115 we employed agar plates and liquid cultures at 25 µmol photons $m^{-2}$ $s^{-1}$ (hereafter abbreviated as
116 µE) of light to avoid stress exposure of potentially affected mutants. On TAP plates, slightly
117 decreased growth was observed for *kea1* only at $\leq 10^4$ spotted cells. This effect was more prevalent
118 if mutant cells were grown autotrophically on HSM plates. Here, genotype-specific differences
119 already emerged at cell numbers between $10^6$ and $10^5$. In both cases, the expression of CrKEA1-
120 YFP in the *kea1* background restored WT growth behavior in all four complementation lines tested
121 (Figure 1E; Supplemental Figure S5B). The slow growth of *kea1* cells replicated well in liquid
122 cultures. Again, the absence of acetate clearly exacerbated this effect; even after nine days of
123 culturing, *kea1* reached only half the cell number as WT and the *CrKEA1-YFP* complemented the
124 *kea1* strain (Figure 1F).

125 *Chloroplast morphology appears altered in kea1 under moderate light conditions*

126 To investigate whether loss of CrKEA1 affects chloroplast organization, we first examined
127 chloroplast morphology using confocal fluorescence microscopy based on chlorophyll
128 autofluorescence (Supplemental Figure S7A, B). Under low light and photoautotrophic conditions
129 (HSM), WT, *kea1*, and *CrKEA1–YFP* complementation lines displayed the characteristic cup-
130 shaped chloroplast typical of Chlamydomonas. When cells were grown under moderate light, *kea1*
131 chloroplasts appeared more heterogeneous, often with less distinct peripheral lobes but a swollen
132 main chloroplast body compared to WT and the complemented strain.

133 To examine these observations at higher resolution, we performed transmission electron
134 microscopy (TEM) on cells grown in HSM under moderate-light conditions (Figure 1G, H;
135 Supplemental Figure S7C).
136 WT and CrKEA1–YFP complemented *kea1* cells consistently displayed the canonical cup-
137 shaped chloroplast with well-defined lobes, regular thylakoid lamellae, and a distinct pyrenoid
138 matrix. In contrast, chloroplasts in *kea1* cells appeared more spheroidal, and the characteristic
139 lobes were not resolved in the analyzed TEM sections, although sectioning effects cannot be
140 excluded. Thylakoid bundles within these chloroplasts also appeared more disorganized compared
141 to the regular lamellar arrays observed in WT.
142 In addition, WT-like pyrenoid structures were not readily identifiable in the TEM sections of *kea1*
143 cells. However, fluorescence imaging indicates that pyrenoid-like structures remain present in
144 most mutant cells (detectable as gap in the autofluorescence). Finally, variation in cell and plastid
145 size was markedly increased in the mutant population, pointing to a loss of volume homeostasis.
146 Together, these observations suggest that loss of CrKEA1 affects chloroplast organization
147 and cellular morphology, particularly under photoautotrophic moderate-light conditions.

148 *kea1 mutants show altered $K^+$ accumulation and slight cytosolic pH changes*

149 To assess whether the growth defects of *kea1* mutants are associated with disturbed ion
150 homeostasis, we quantified the elemental composition of whole cells grown in TAP medium at 25
151 µE using total reflection X-ray fluorescence (TXRF; Holzner et al., 2026).
152 Elemental profiles on a per-cell basis were broadly consistent with previously reported
153 values (Merchant et al., 2020; Schmollinger et al., 2021) and showed elevated levels of several
154 elements in the *kea1* mutant, consistent with its increased cell size (Supplemental Figure S8A).
155 However, after normalization to cell volume, only $K^+$ levels remained significantly elevated (1.85-
156 fold) in *kea1*, whereas differences in other elements did not reach statistical significance (Figure
157 2A). The complementation line displayed intermediate $K^+$ levels between mutant and WT.
158 Because IE KEA transporters mediate $K^+/H^+$ exchange across the chloroplast envelope,
159 their disruption is expected to primarily alter intracellular ion distribution rather than total cellular
160 $K^+$ content. Whole-cell measurements therefore likely underestimate the extent of ionic
161 perturbations within subcellular compartments.

162 Alkali cation/$H^+$ antiporters can alter pH and/or cation homeostasis (Sze and Chanroj, 2018). To
163 determine whether the $K^+$ changes in *kea1* are accompanied by altered proton homeostasis, we
164 next measured cytosolic pH using the ratiometric fluorescent dye BCECF, which has been
165 previously established for pH measurements in Chlamydomonas (Braun & Hegemann, 1999; Pang
166 et al., 2023). BCECF-AM enters the cell in an esterified form and becomes trapped in the cytosol
167 after esterase cleavage, enabling ratiometric pH determination based on the fluorescence excitation
168 ratio (490/440 nm; Figure S8B). Using this approach, we observed a slightly elevated cytosolic
169 pH in the *kea1* mutant compared to WT (Figure 2B). If loss of CrKEA1 leads to partial retention
170 of $K^+$ within the chloroplast, the cytosol may experience a relative $K^+$ deficit and trigger increased
171 proton extrusion via plasma membrane $H^+$-ATPases to drive $K^+$ uptake. This could contribute to
172 the mildly elevated cytosolic pH observed in the *kea1* mutant.
173 While BCECF does not report the stromal pH, these measurements indicate that
174 perturbation of chloroplast $K^+/H^+$ exchange in *kea1* is accompanied by measurable changes in
175 cytosolic proton balance. Together with the altered $K^+$ levels detected by TXRF, these results
176 support the conclusion that loss of CrKEA1 leads to a broader disturbance of cellular ion
177 homeostasis.

178 *Loss of CrKEA1 results in a light-dependent decrease in photosynthetic performance*

179 The observed growth defects may correlate with impaired photosynthetic performance.
180 Hence, we recorded electron transport rates (ETR) during step-wise light intensity
181 (photosynthetically active radiation; PAR) increases. Interestingly, once light intensities surpassed
182 the moderate range ≥80 PAR, *kea1* cells revealed lower ETR, consistent with increased light
183 susceptibility compared to WT and the complementation line (Figure 3A). A similar effect was
184 observed in drop cultures. While the maximum quantum efficiency of PSII ($F_v/F_m$) did not differ
185 between genotypes at 0–20 µE, stepwise increases in light intensity (every hour) caused a stronger
186 decline in $F_v/F_m$ in *kea1* compared to WT and the complementation line (Figure 3B). The same
187 trend was observed after long-term exposure (4 days) to 25 or 100 µE in *kea1*, compared with the
188 WT and four independent *CrKEA1-YFP* strains (Supplemental Figure S5B).
189 For additional insight, we established a light intensity shift routine for liquid cultures.
190 Initially, $F_v/F_m$ was determined in all three genotypes grown at 25 µE either in HSM or TAP media.
191 Regardless of the growth media used, no clear differences emerged across the strains. However, if

192 the same genotypes were shifted to standard moderate light conditions (100 µE; Bialevich et al.,
193 2022) for 24 h, a clear $F_v/F_m$ drop was noticeable for the mutant but not for the WT and all six
194 *CrKEA1-YFP* lines measured (Figure 3C; Supplemental Figure S5C). Subsequent incubation for
195 24 h at 25 µE restored $F_v/F_m$ to baseline levels.

196 To further investigate the physiological basis of the reduced ETR and $F_v/F_m$ values
197 observed under moderate light, we assessed non-photochemical quenching (NPQ) induction and
198 recovery from photoinhibition. Because NPQ capacity in Chlamydomonas depends on the high-
199 light–inducible LHCSR3 protein (Peers et al., 2009), NPQ was measured both in low-light–grown
200 cultures and in cultures subjected to repeated brief high-light treatments to induce LHCSR3
201 expression. Under both conditions, *kea1* cells displayed reduced NPQ induction compared to WT
202 and the complementation line, although NPQ increased in all strains following high-light
203 pretreatment (Figure 3D).

204 We next examined recovery from photoinhibition by exposing cultures to high-light
205 treatments that caused a defined decrease in $F_v/F_m$, followed by transfer to low light while
206 monitoring PSII recovery over time. In these experiments, WT and the complementation line
207 recovered more rapidly than the *kea1* mutant (Figure 3E).

208 In summary, *kea1* mutants are highly light sensitive and show clear photosynthetic defects,
209 which are fully rescued by *CrKEA1-YFP* expression, confirming loss of CrKEA1 as the causative
210 mutation. While low light intensities (25 µE) are mostly permissive for *kea1*, PSII efficiency
211 declines sharply under moderate light (~100 µE). Consistent with this, *kea1* cells display reduced
212 NPQ capacity and recover more slowly from photoinhibition, indicating that the mutant is less
213 effectively protected from light-induced damage and has a reduced capacity to restore PSII activity
214 after stress.

215 *Flow cytometry shows increased cell sizes for kea1 shifted from low to moderate light*

216 Next, we examined the response of TAP and HSM cultures to the light shift using flow
217 cytometry (Figure 3F; Supplemental Figure S9). Regardless of the growth medium, *kea1* cells
218 were slightly larger in size based on FSC-A values at low light (25 µE). 48 h after the shift to
219 moderate light (100 µE), cell size increased for both media across all genotypes. However, *kea1*
220 cultures showed the strongest increase in cell size and broadening of the size distribution. This
221 phenotype was rescued in all six complementation lines examined (Supplemental Figure S5C).

222 After 48 h of moderate light treatment, calibration indicated average volume increases of 19% in
223 TAP and 23% in HSM for WT, 9% in TAP and 19% in HSM for the *CrKEA1-YFP* line, and 97%
224 in TAP and 67% in HSM for *kea1* (Supplemental Table S2). Using SSC-A as a proxy for cell
225 complexity, changes in the *kea1* mutant (82%) by far exceeded those in WT (-4%) and the
226 complemented line (6%) under TAP conditions. A similar trend was observed in HSM, with
227 complexity increases of 52% for *kea1*, 19% for WT, and 4% for the *CrKEA1-YFP* line
228 (Supplemental Table 3).

229 *Transcriptome profiling during light acclimation reveals that the absence of KEA1 alters ribosome*
230 *biogenesis, plastid fission, and cell cycle regulation*

231 Given the impaired physiological performance of *kea1* mutant cells upon shift into
232 moderate light, we sought to identify biological processes affected by the loss of *CrKEA1* through
233 characterizing the underlying transcriptional responses. To this end, we performed RNA
234 sequencing (RNA-seq) on cultures subjected to the established light shift regime. Cells grown
235 under low light (LL, 25 µE) were exposed to moderate light (ML, µE) for 8 h, followed by a 24 h
236 low-light recovery phase (RL, 25 µE) (Figure 4A). The experiment was set up with TAP medium
237 to ensure that *kea1* cells experience stress but not the exacerbated defects observed in HSM. Ribo-
238 depleted libraries were prepared to capture the full extent of transcriptional changes, including
239 organellar transcripts.

240 For physiological validation of the light treatment, we again recorded $F_v/F_m$ at each
241 sampling point. While there was no genotype-specific difference at the onset of the experiments
242 i.e., at 25 µE, only 8 h at 100 µE induced clear PSII photoinhibition ($F_v/F_m$ drop) in *kea1* mutants.
243 By contrast, WT cells readily acclimated to the changing light regime (Figure 4A; Supplemental
244 Figure S10A). Following the RL phase, PSII quantum yield was fully restored in all genotypes.

245 Multidimensional scaling (MDS) showed tight clustering of replicates ($n$=4) and a stronger
246 genotype separation under ML (Supplemental Figure S10B). Consistent with this, the number of
247 significantly differentially expressed genes (DEGs, adjusted p-value < 0.05) under LL (1419
248 DEGs) went up >6-fold under ML (7632 DEGs) but back down at RL conditions (1370 DEGs)
249 (Figure 4A; Supplemental Figure S10C, D; Supplemental Table S4). In addition, ML DEGs were
250 more strongly deregulated i.e., more DEGs above the $|\log_2 FC| \geq 1$ threshold than under other light
251 conditions.

252 Gene Ontology (GO) enrichment analyses highlighted a coordinated shift in cellular
253 programs under ML (Figure 4B; Supplemental Table S5): Upregulated DEGs were strongly
254 enriched for *ribosome biogenesis*, including *rRNA processing*. Both categories contained cytosolic
255 and plastid ribosome biogenesis components. Downregulated categories included *cell cycle*, *DNA*
256 *replication*, *chromatin organization*, and *microtubule-based processes*, which are partly
257 intertwined.

258 Consistent with this, these trends were confirmed by a detailed analysis of transcript
259 changes. For the heatmaps shown in Figures 4C and 4I, again only significantly differentially
260 expressed genes (adjusted p value < 0.05) were considered for interpretation; genes that did not
261 meet this threshold in a given condition are indicated in black. Under these conditions, a broad
262 upregulation of ribosome-related genes was observed when *kea1* cells were exposed to moderate
263 light (Figure 4C). By contrast, cell cycle–related genes were by and large downregulated in *kea1*
264 cells under these light conditions (Figure 4D). While *CDKA1*, the major driver of the G1/S
265 transition (Tulin and Cross, 2014), was unchanged, multiple key regulators of the Chlamydomonas
266 cell cycle were expressed below WT-level in *kea1*: Expression of genes controlling S/M transitions
267 by blocking spindle formation was strongly decreased, including *CDKB1(2)* and its activating
268 cyclins (*CYCA1*, *CYCB1*). Three of the D-type cyclins, which mediate G1/S entry (Bisova et al.,
269 2005), were mildly reduced (~2-fold for *CYCD3, 5*). In addition, transcript accumulation for both
270 *CDKG1*, which becomes induced when cells reach sufficient size for division (Li et al., 2016), and
271 for *MAT3*, a retinoblastoma homolog regulating the commitment to division (Umen and
272 Goodenough, 2001), were slightly diminished. Together, these changes provide evidence that the
273 cell cycle entry and S/M cycling might be affected in the *kea1* mutants (Supplemental Figure
274 S10E).

275 Interestingly, most transcripts associated with the GO term *plastid fission* were markedly
276 reduced in light-shifted *kea1* cells (Figure 4E), suggesting a link between KEA1 function in the
277 plastid envelope membrane and chloroplast division control in algae.

278 *Absence of KEA1 suppresses PhANGs but triggers an induction of PGE and protein homeostasis*
279 *genes*

280 Arabidopsis *kea1kea2* mutants display delayed chloroplast biogenesis caused by activation
281 of GUN1-dependent retrograde signaling, which suppresses the expression of GOLDEN2-LIKE

282 transcription factors and their downstream gene cluster of photosynthesis-associated nuclear genes
283 (PhANGs; DeTar et al., 2021). Hence, we curated a *PhANG* list for Chlamydomonas. Interestingly,
284 *kea1* cells showed a clear repression of genes encoding for light-harvesting complexes,
285 photosystem subunits, and chlorophyll biosynthesis enzymes under ML (Figure 4F), which is
286 reminiscent of the response described for *kea1kea2* plant mutants (DeTar et al., 2021).
287 Furthermore, among downregulated genes, also photosynthesis-related GO terms were enriched
288 in the Chlamydomonas *kea1* mutant (Figure 4B). By contrast, plastid-encoded photosynthesis
289 genes were largely unaffected, though transcripts for plastid transcription/translation components
290 (e.g., RNA polymerase subunits, ribosomal proteins), essential for plastid gene expression (PGE),
291 were elevated in *kea1* compared to WT (Figure 4G; Supplemental Figure S10G). This suggests
292 that the photosynthetic decline may not only arise from a transcriptional repression within the
293 plastid, but in addition from defective translation, consistent with the general enrichment of
294 ribosome biogenesis transcripts.

295 Other DEG categories were more selective. Chloroplast-encoded genes for chlorophyll
296 biosynthesis were unchanged in *kea1* (Supplemental Figure S10G). Likewise, *HMOX* and *GUN4*,
297 which regulate tetrapyrrole and bilin synthesis relevant for retrograde signaling in
298 Chlamydomonas (Duanmu et al., 2013), were unaffected. However, bilin-synthesis gene *PCYA*
299 was upregulated under ML (Figure 4H). Chlamydomonas lacks close *GOLDEN2-LIKE*
300 *transcription factor* homologs and probably relies mainly on a bilin-derived retrograde signaling
301 pathway to repress PhANGs and facilitate acclimation (Duanmu et al., 2013; Richter et al., 2023).
302 Hence, the observed *PCYA* induction likely contributes to the *PhANG* suppression observed in
303 *kea1*.

304 Next, we examined nuclear genes implicated in protein homeostasis, ROS defense, and
305 photoprotection (Figure 4H). Plastid-encoded quality control proteins, namely *PsbN* involved in
306 PSII repair and the proteases *ClpP* and *FtsH*, were mildly upregulated in *kea1* under ML, while
307 nuclear-encoded PSII repair factors (*HCF136*, *TerC1*, *ALB3*, *PsbW*, *PsbY*; Plöchinger 2016)
308 showed no consistent change with a tendency for down-regulation. Several ROS-related genes
309 (*GPX5*, *MBS*, *SOR1*, *VTC2*) were upregulated in the mutant under ML, whereas photoprotection
310 factors (qE/NPQ) showed mixed patterns: *PSBS* transcripts were elevated in the mutant, but
311 *LHCSR* induction was attenuated relative to WT, consistent with the reduced NPQ observed in
312 *kea1* (Figure 3D). In turn, *SPA1*, a component of the E3 ubiquitin ligase complex (CUL4-DDB1-

313 LRS1-SPA) involved in repression of PSBS- and LHCSR-mediated qE (Gabilly et al., 2019;
314 Aihara et al., 2019), was downregulated, implying altered control of qE responses in *kea1*.
315 Because higher expression of protein quality control genes (*ClpP* and *FTSH*) was observed
316 in the plastid, we also analyzed markers of the chloroplast unfolded protein response (cpUPR).
317 Genes encoding cpUPR components, including *VIPP2* (sensing), *MARS1* (signaling), and markers
318 such as *CLPB3*, *DEG1C*, *FTSH2*, *HSP22E/F*, and *HSP70B* (Ramundo et al., 2014; Perlaza et al.,
319 2019; Theis et al., 2020), were consistently upregulated in *kea1* compared to WT (Figure 4H), in
320 most cases already at LL conditions i.e., 25 µE.

321 *Expression of ion transporters in kea1 is altered under low and moderate light*

322 When analyzing genes upregulated ($\log_2 FC \geq 1$) in *kea1* LL conditions, the GO term
323 potassium transport (GO:0006813) was significantly enriched (Supplemental Table S5). Within
324 this group, several HAK/KUP/KT-type high-affinity $K^+$ transporters (*HAK2*, *HAK4*) and
325 $Na^+/SO_4^{2-}$ transporter-like genes (*SLT1-SLT3*) showed elevated transcript levels in the mutant
326 compared to WT (Figure 4I, Supplemental Figure S10F). These transporter families have
327 previously been linked to $K^+$ and sulfate acquisition and to the maintenance of cellular ion balance
328 (Li et al., 2023; Pootakham et al., 2010).
329 Inspection of the complete gene set within the $K^+$-transport category revealed that
330 expression changes persisted or became more pronounced under moderate light (ML). The same
331 transporters that were induced under LL remained among the most strongly upregulated genes
332 under ML, except *HAK2*, which decreased relative to WT. Additional transporters, including
333 *HAK3* and *NAK1*, the sole $Na^+/K^+$-ATPase-like pump homolog in Chlamydomonas, were also
334 induced. NAK1 and HAK-like proteins respond to low- $K^+$ and saline stress and mediate cytosolic
335 $K^+$ and $Na^+$ homeostasis (Li et al., 2023). Hence, their upregulation in *kea1* suggests a disturbance
336 in cellular ion homeostasis and activation of low-$K^+$–responsive pathways, possibly reflecting
337 altered $K^+$ partitioning causing cytosolic $K^+$ deficiency or impaired ion signaling between the
338 chloroplast and cytosol (Figure 4I).
339 Across the light-shift experiment, *SLT* and *HAK* family members, along with other
340 significant genes from this GO term, followed a similar trend in *kea1* (and partially in WT) in
341 response to the light treatment: transcript levels increased under ML and declined again during

342 recovery (RL), but transcription was constantly higher in the *kea1* mutant than in the WT
343 (Supplemental Figure S10F).
344 *KCN11*, a tonoplast $K^+$ channel required for osmoregulation, also showed significantly elevated
345 transcript levels ($\log_2$FC = 0.43) in *kea1* under ML (Figure 4I). The upregulation of KCN11 in
346 *kea1* thus supports the interpretation that loss of *CrKEA1* perturbs osmotic balance, consistent with
347 broader alterations in ion homeostasis.
348 In summary, loss of *CrKEA1* triggers a multifaceted transcriptional response pointing
349 towards a dual role for CrKEA1-dependent ion homeostasis in maintaining chloroplast translation
350 capacity and safeguarding protein folding.

351 *Species-Specific Consequences of KEA1 - Loss for Plastid and Cell Cycle Regulation*

352 Having observed similar transcriptional upregulation of ribosome biogenesis genes in both
353 species upon *KEA* loss, we aimed to explore similarities and differences in transcriptomic
354 responses between Chlamydomonas and Arabidopsis IE *KEA* knockouts. To this end, we re-
355 analyzed RNA-seq data from Arabidopsis WT and *kea1kea2* mutants (DeTar et al., 2021;
356 Supplemental Table S6) and compared it with the RNA-seq data from the Chlamydomonas *kea1*
357 mutant. To identify genes commonly or uniquely regulated in response to IE *KEA1* disruption
358 across species, we mapped Chlamydomonas DEGs to their closest Arabidopsis homologs and
359 categorized the results into three groups: shared DEGs (genes differentially expressed in both
360 species) and species-specific DEGs (Supplemental Table S7).
361 Notably, transcriptomic comparisons between Arabidopsis and Chlamydomonas are
362 inherently constrained by major biological and experimental differences between the two systems,
363 including fundamental differences in physiology, cellular organization, and organism-specific
364 growth conditions (Julca et al., 2023). The cross-species comparison should therefore be
365 interpreted as an exploratory analysis aimed at identifying broadly conserved or lineage-specific
366 responses to IE KEA loss rather than as a strict one-to-one comparison of transcriptional
367 regulation. Nonetheless, similarities observed despite these differences may highlight robust
368 aspects of the cellular response to disrupted chloroplast ion homeostasis.
369 GO term enrichment analyses on these categories (Figure 5A; Supplemental Table S8)
370 revealed that DEGs involved in ribosome biogenesis were largely shared between the two species,
371 indicating a conserved stress response linked to impaired rRNA maturation. In contrast, DEGs

372 related to the cell cycle were exclusively found in Chlamydomonas, suggesting a lineage-specific
373 consequence of *KEA1* loss on cell division control.

374 The Arabidopsis-specific DEGs were enriched for GO terms associated with, i.e.,
375 responses to various stimuli, including light, red and far-red light signaling, wounding, and
376 regulation of multicellular development, consistent with the plants' complex tissue architecture
377 and photomorphogenic signaling networks (Figure 5A).

378 A direct comparison at the level of DEGs further confirmed that ribosome biogenesis genes
379 are upregulated in both species (Figure 5B). However, cell cycle–related genes are strongly
380 downregulated in Chlamydomonas but not significantly altered in Arabidopsis. Interestingly, most
381 genes related to plastid fission showed opposite trends: they were downregulated (*MINE*, *MIND*,
382 *FTSZ1*, *ARC5*, *ARC6*) in Chlamydomonas but many slightly upregulated in Arabidopsis (*FTSZ1*,
383 *ARC6*, which are conserved in both) or not-significant (*MIND*). However, key plastid division
384 genes, like *PDV1* and *PDV2*, which are unique to land plants and determine plastid division rate
385 (Miyagishima et al., 2006; Okazaki et al., 2009, Holtsmark et al., 2013), and *MINE* and *ARC5*,
386 were slightly down-regulated in Arabidopsis.

387 *Plastid rRNA processing is impaired in both At and Cr kea1 mutants*

388 Given the transcriptional upregulation of ribosome biogenesis genes in both Arabidopsis
389 and Chlamydomonas IE *KEA* mutants (Figure 5B), we examined whether loss of *CrKEA1* in algae
390 also disrupts plastid rRNA maturation, leading to the accumulation of unprocessed rRNA
391 precursors as observed in plants (DeTar et al., 2021; DeTar et al., 2022). Notably, plastid rRNA
392 processing differs between the two lineages in several important aspects: 1) Arabidopsis generates
393 a 4.5S rRNA fragment from the 23S precursor, whereas Chlamydomonas instead produces the
394 distinct 7S and 3S fragments cleaved from the opposite end (Holloway and Herrin, 1998; Ahmed
395 et al., 2016; Schmid et al., 2024); 2) Chlorophytes employ much more octotricopeptide repeat
396 (OPR) RNA-binding proteins (RBP) while plants rely heavily on pentatricopeptide repeat (PPR)
397 proteins (Small et al., 2023). However, both systems rely on precise cleavage of large precursor
398 transcripts into functional ribosomal RNAs, which involves temporal sequence-specific RNA-
399 RBP interactions (Supplemental Figure S11).

400 To test for stromal rRNA maturation defects in Chlamydomonas, we analyzed total RNA
401 from *kea1* and WT cultures using rRNA sequencing. Initially, all stromal rRNA reads from *kea1*

402 and WT were aligned akin to previous studies (Hotto et al., 2015; Castandet et al., 2016). This
403 approach revealed increased read coverage within intergenic regions in *kea1*, particularly in the
404 7S and 3S regions derived from the 23S precursor. Since these fragments are removed during
405 rRNA maturation, their high abundance in *kea1* indicated mutant-specific accumulation of
406 unprocessed rRNA intermediates (Figure 6A, Supplemental Figure S12A, B). To corroborate these
407 observations, we carried out RNA blots employing stromal rRNA-specific probes. Indeed, a clear
408 accumulation of the 7S-3S-23S precursor was specifically observed in *kea1* cells (Figure 6B,
409 Supplemental Figure S13A, B). Splicing defects did not change with light shifts, but they were
410 less abundant in cells grown in TAP medium.

411 In summary, results from our RNA analyses suggest that despite significant differences in
412 rRNA structures and processing pathways between algae and land plants, the importance of IE
413 KEAs for seamless plastid rRNA processing is functionally conserved between chlorophytes and
414 streptophytes.

415 *Functional conservation of IE KEA transporters between algae and higher plants*

416 The rRNA processing phenotypes observed in plants and green algae suggest functional
417 conservation of IE KEAs across the green lineage. We therefore tested whether CrKEA1 can
418 substitute for its homologs AtKEA1/2 in Arabidopsis. Despite substantial amino acid sequence
419 divergence between CrKEA1 and AtKEA1, structural predictions generated with AlphaFold3
420 (DeepMind; Abramson et al., 2024) indicate a broadly conserved domain architecture (Figure 6C;
421 Supplemental Figure S14A-C; Gulati et al., 2024). Initially, we cloned full-length *CrKEA1* with a
422 C-terminal YFP. The finished construct *CrKEA1-YFP* was transformed into the *kea1-1kea2-1*
423 (hereafter simply *kea1kea2*) Arabidopsis mutant allele (Kunz et al., 2014). Several independent
424 transgenic *CrKEA1-YFP* lines exhibited robust complementation i.e., growth, leaf area, fresh
425 weight, and photosynthetic performance ($F_v/F_m$ and ETR) were restored close to WT levels (Figure
426 6D; Supplemental Figure S15). Subsequent immunoblotting confirmed the accumulation of
427 CrKEA1-YFP in the transgenic lines at the expected apparent size of ~140 kDa (Figure 6E).

428 Next, we conducted RNA blots with WT, *kea1kea2*, and *CrKEA1-YFP* complemented lines
429 and found that CrKEA1-YFP restores plastid 23S rRNA processing (Figure 6F).

430 Together, these findings demonstrate that despite a billion years of divergence, CrKEA1
431 retains sufficient functional similarity to AtKEA1/2, which reveals a strong evolutionary

432 conservation of $K^+/H^+$-mediated effects on ribosome biogenesis. Curiously, when expressed in
433 Arabidopsis, CrKEA1-YFP localized in discrete, rod-like structures, whereas the endogenous
434 AtKEA1-YFP appeared in discrete spots (Figure 6G).

435 *Comparison of co-expression networks reveals a divergent cell cycle embedding in Arabidopsis*
436 *and Chlamydomonas*

437 Since the GO terms *cell cycle* and *plastid fission* were affected in the Chlamydomonas
438 mutant but not in Arabidopsis, we carried out an in-depth comparison between the respective co-
439 expression networks (Figure 7A). Direct co-expression involves "*gene to gene*" interactions, while
440 secondary co-expression involves "*gene to intermediary gene to gene*" interactions. In the
441 Chlamydomonas co-expression network (ML condition based), *ARC5*, *ARC6*, and *MIND,* all
442 scoring a $\log_2$FC < -2, were found to be secondary neighbors in a shared cluster with cell cycle
443 genes: e.g., *MIND* with the key *cell cycle* gene *CDKB1(2)* but also *ARC5* with *TOPII*, *TPX2*,
444 *AUR2*, *MCM5*, *WEE1* that were similarly downregulated with a $\log_2$FC < -1. This indicates that
445 both biological processes have tightly co-expressed interactions resulting in unidirectional
446 expression changes.

447 Interestingly, in Arabidopsis co-expression networks, *cell cycle* genes show little to no
448 regulatory concordance with *plastid fission* genes. Transcripts of *ARC5*, *PDV1*, and *PDV2*
449 displayed $\log_2$FC values between -0.75 and 0, while *FTSZ2-1*, *FTSZ2-2*, *ARC6*, *MSL2*, *MSL3*,
450 *MCD1*, *KASI*, *MURE*, and *AT2G21280* (*GC1*) ranged between 0 and 0.75, indicating that
451 regulating these genes in response to the loss of IE *KEA* had little biological significance for
452 Arabidopsis. While certain genes involved in Arabidopsis chloroplast division were regulated with
453 absolute values higher than a $|\log_2\text{FC}|$ of 0.75 (ie. upregulated *YLMG1-1* and *FTSHi1*), they were
454 not concertedly downregulated with *cell cycle* genes as in Chlamydomonas.

455 To further substantiate co-expression between *cell cycle* and *plastid fission* genes, we
456 plotted the percentage of co-expressed interactions (direct and secondary) for each species (Figure
457 7B). Within the Arabidopsis co-expression network, 5.3% (4 genes) are direct interactors, while
458 94.7% (72 genes) are secondary interactors. However, none of these genes were strongly
459 ($|\log_2\text{FC}| \geq 0.75$) differentially expressed in *kea1kea2* mutants. For Chlamydomonas, 100% (4
460 genes) of the genes are involved in secondary interactions, with 75% (*ARC5*, *ARC6, MIND*)
461 showing co-regulated downregulation.

462 To identify orthologs of *cell cycle* genes in Chlamydomonas and Arabidopsis, we used an
463 orthogonal approach building on CoNekT (Figure 7C). When comparing co-expression clusters of
464 TOPII, we found several *cell cycle* genes were orthologs between species. *ROW1*, *MCM10*,
465 *PAKRP1L*, *POK1*, *POK2*, *ZCF125* were found to have orthologs within Chlamydomonas that were
466 not annotated by best BLAST hits. Within this gene family, three Chlamydomonas genes were
467 grouped together with seven genes. For *plastid fission* genes, no apparent similarity between
468 Chlamydomonas and Arabidopsis clusters were found. This analysis also indicates that the
469 biological process *cell cycle* in Chlamydomonas showed certain similarities with Arabidopsis.

470 *Single-Cell Time-Lapse Imaging Reveals Cell Cycle irregularities in kea1*

471 *kea1* mutant cells displayed pronounced size distribution differences in micrographs and
472 when analyzed by flow cytometry (Figure 3F). In addition, coordinated downregulation of cell
473 cycle and chloroplast division genes was observed in the *kea1* transcriptome (Figure 4D, E). In
474 Chlamydomonas, cell division proceeds via a multiple fission cycle, in which cells undergo n
475 divisions (S/M phase) into $2^n$ daughter cells after a prolonged G1 phase. The size of the mother
476 cell determines the number of divisions resulting in 2, 4, 8, 16, etc. equally sized daughter cells
477 (Figure 8A; Cross and Umen, 2015).

478 The intrinsic heterogeneity of batch cultures poses substantial challenges for the
479 identification of cell cycle stage-specific defects. To overcome these limitations, we developed a
480 live-imaging platform capable of tracking individual cells over several days. Cells were applied to
481 a custom-made, biologically inert hydrogel with multiple chambers embedded in a flow cell chip
482 (Figure 8B). Our design allows for tight temperature- and light-control, constant medium flow,
483 nutrient diffusion, and continuous imaging throughout Chlamydomonas cell division cycles. In
484 addition, the multiple chambers situated on a single chip enabled simultaneous side-by-side growth
485 and monitoring of WT and *kea1* mutant strains under the exact same controlled culturing
486 conditions in TAP medium at 25 µE (Figure 1G).

487 WT cells displayed regular and symmetric division with high fidelity, verifying ideal and
488 well-suited growth conditions in our continuous flow cell chip setup (Figure 8C; Supplemental
489 Figure S16A). By contrast, our analysis revealed several key differences in the mutant compared
490 to WT: *kea1* cells were significantly larger than WT cells during every segment of the G1-division
491 cycle (Figure 8D). Interestingly, the elevated volume of *kea1* cells can be traced back to the mid-

492 G1 phase (Supplemental Figure S16B), when mutant cells exhibit a significantly higher volume
493 increase than WT. Additionally, mutant cells not only remained longer in the G1 phase (Figure
494 8E) but also took longer to complete the S/M phase (Figure 8F).

495 Upon closer examination, specific cytokinesis defects were observed more frequently in
496 *kea1* mutants: 1) Divisions often produced daughter cells of unequal size (Figure 8G), hinting at a
497 misplaced division plane. Further analysis of mutant daughter cells revealed that these birth
498 volume deviations did not affect subsequent G1-division cycle length differences compared to
499 those of WT daughters (Supplemental Figure S16C). 2) Remerging of seemingly already divided
500 cells multiple hours into the G1 phase was observed in approximately 3% of all *kea1* divisions but
501 was never detected in WT (Figure 8H). Remerged cells divided into 3 or 5 daughter cells after
502 completing their G1 phase (Supplemental Figure S16A), possibly due to two coexisting nuclei in
503 a single remerged cell.

504 To further quantify division defects, we determined the fraction of mother cells that failed
505 to produce viable dividing progeny (including rupture, disintegration, or non-dividing daughter
506 cells), which occurred more frequently in kea1 (28%, n = 60) than in WT cells (19%, n = 57).

507 Our single-cell imaging revealed pronounced defects in cell cycle progression and division
508 fidelity, confirming the transcriptomic observations.

509 **Discussion**

510 Plastid integrity relies on tightly controlled ion fluxes across the inner envelope membrane.
511 Our findings establish CrKEA1 as the functional counterpart of AtKEA1/2 in Arabidopsis, adding
512 experimental support to the hypothesis that KEA-mediated $K^+/H^+$ exchange at the plastid envelope
513 represents an ancient and conserved feature of plastid physiology that likely emerged early during
514 plastid evolution. Loss of *CrKEA1* is associated with alterations in plastid morphology and reduced
515 photosynthetic performance under moderate-light conditions, defects in plastid rRNA maturation,
516 and delayed cell-cycle progression. Together, these phenotypes reveal both conserved and lineage-
517 specific aspects of KEA function across the green lineage (Figure 9).

518 In Arabidopsis, disruption of *AtKEA1/2* causes increased cellular $K^+$ levels, fragile
519 chloroplasts, impaired photosynthesis, and growth (Kunz et al., 2014; Aranda-Sicilia et al., 2016).
520 We observed related phenotypes in *kea1* mutants, including altered ion balance, growth delay,
521 changes in chloroplast morphology, and reduced photosynthetic efficiency at increased irradiance.

522 These parallels suggest that KEA activity at the plastid envelope plays a broadly conserved role in
523 maintaining the ion homeostasis required for plastid function. The strong conservation of this role
524 is further supported by cross-species complementation, in which CrKEA1 restored growth,
525 photosynthesis, and rRNA processing in Arabidopsis *kea1kea2* mutants. However, it remains
526 challenging to distinguish primary consequences of impaired plastid ion transport from
527 downstream physiological responses triggered by altered photosynthetic performance and
528 metabolic status.

529 Despite this limitation, our findings accentuate the potentially fundamental role of IE KEAs
530 in supporting cellular biochemistry by maintaining pH and ion homeostasis in phototropic
531 eukaryotes — a function that may have been conserved since the last common ancestor, likely
532 persisting through more than a billion years of evolutionary divergence (for molecular clock, see
533 Strassert et al., 2021 and Bierenbroodspot et al., 2025).

534 Consistent with this deep evolutionary conservation are the parallels between plants and
535 algae in the role of KEA transporters in plastid rRNA maturation. In Arabidopsis, loss of
536 AtKEA1/2 disrupts rRNA processing and plastid translation (DeTar et al., 2021). Similarly,
537 Chlamydomonas *kea1* mutants accumulated unprocessed 23S-derived precursors, in accordance
538 with impaired maturation. Although the 23S rRNA maturation pathways differ between algae and
539 plants — Chlamydomonas generates unique 7S and 3S fragments, whereas Arabidopsis produces
540 a separate 4.5S rRNA from the opposite end of the 23S precursor — the accumulation of immature
541 rRNA in Chlamydomonas *kea1* closely mirrors the maturation defects seen in Arabidopsis
542 *kea1kea2* (DeTar et al., 2021; DeTar et al., 2022). Structural work offers a mechanistic basis for
543 this observation, showing that $K^+$ and magnesium ions are required to stabilize rRNA and the large
544 ribosomal subunit (Nierhaus, 2014; Rozov et al., 2019; Klein et al., 2004). Ion imbalance in *kea1*
545 mutants could potentially destabilize rRNA precursors and interfere with their proper processing,
546 or indirectly affect maturation through feedback from defective ribosome assembly (DeTar et al.,
547 2021). Together, our findings strengthen the model that ion imbalance destabilizes rRNA
548 secondary structures and disrupts ribosome biogenesis across systems, despite lineage-specific
549 differences in processing outcomes.

550 Transcriptomic profiling revealed a conserved upregulation of ribosome biogenesis genes
551 and downregulation of PhANGs in *kea1*, mirroring the Arabidopsis *kea1kea2* response (DeTar et
552 al., 2021). In both species, repression of photosynthetic gene expression likely reflects a protective

553 adjustment to plastid dysfunction. In Arabidopsis *kea1kea2* mutants, the retrograde response is a
554 GUN1-mediated GOLDEN2-LIKE (GLK1/GLK2) transcription factor suppression to delay
555 chloroplast biogenesis, thereby minimizing photo-oxidative damage until stress has been resolved
556 (DeTar et al., 2021). However, this regulatory logic is unlikely to apply to Chlamydomonas: 1)
557 GLK1/2 emerged as a hub controlling the genetic networks that underpin chloroplast
558 differentiation and photomorphogenesis only in zygnematophytes (Dadras et al., 2023), and 2)
559 although GUN1 is evolutionarily ancient, its role in retrograde signaling is thought to have arisen
560 after streptophyte algae diverged from chlorophytes (Honkanen and Small, 2022). Thus, PhANG
561 suppression in Chlamydomonas must rely on different upstream cues. In *kea1*, where we also
562 found induced ROS-responsive transcripts, an upregulation of *PCYA*, a bilin-synthesis gene, points
563 to tetrapyrrole-derived retrograde signals to repress PhANGs during plastid stress as a coping
564 mechanism (Duanmu et al., 2013).

565 Because the compared datasets were generated under different experimental contexts and
566 in distinct organisms, these similarities should be interpreted as indicative of broadly conserved
567 stress responses rather than direct regulatory equivalence.

568 The concurrent induction of $Na^+/SO_4^{2-}$ (SLT1–3;Pootakham et al.,2010) and $K^+$
569 transporters (particularly *HAK*, *NAK;* Li et al., 2023) together with the altered expression of other
570 ion pumps, exchangers and channels, suggests that disruption of plastid $K^+/H^+$ exchange triggers
571 broader adjustments in cellular ion homeostasis. These regulatory patterns may reflect systemic
572 compensatory responses to altered ion gradients or membrane potentials resulting from impaired
573 $K^+/H^+$ exchange at the plastid envelope. Increased sulfate uptake could further support glutathione
574 biosynthesis, mitigating oxidative stress associated with disturbed ion balance (Niyogi, 1999;
575 Zhang et al., 2004). Also, the tonoplast $K^+$ channel *KCN11* was slightly upregulated. Interestingly,
576 *kcn11* mutants display growth defects under nitrogen limitation, including enlarged cell size (Xu
577 and Pan, 2020; Fauser et al., 2022; Vilarrasa-Blasi et al., 2024). These findings point towards the
578 functional coupling of $K^+$ and sulfate fluxes as part of the wider physiological consequences of
579 disrupted KEA-mediated ion transport in Chlamydomonas. In addition to these conserved features,
580 IE *KEA* loss in Chlamydomonas exhibited lineage-specific consequences. *kea1* mutants showed
581 constitutive induction of the MARS1-dependent chloroplast unfolded protein response (cpUPR;
582 Perlaza et al., 2019). Unlike Arabidopsis, where cpUPR markers were absent or even
583 downregulated (e.g., *CLPB3*) in *kea1kea2* (DeTar et al., 2021), Chlamydomonas activates these

584 stress pathways constitutively (already under low light), consistent with destabilized stromal
585 protein homeostasis as soon as ion balance is disrupted by loss of *CrKEA1*. This points to a lineage-
586 specific strategy: whereas multicellular plants can attenuate plastid protein synthesis and postpone
587 chloroplast biogenesis to avoid protein aggregation, the single-celled alga Chlamydomonas cannot
588 completely postpone chloroplast function without jeopardizing survival. Thus, the unicellular alga
589 must maintain translation in its single essential plastid and instead relies on cpUPR pathways to
590 counteract misfolding and aggregation (Dogra et al., 2019; Perlaza et al., 2019; Richter et al.,
591 2023).

592 Further characteristic observed in Chlamydomonas *kea1* mutants were enlarged cells, an
593 extended G1 phase, irregular cytokinesis, and strong downregulation of cell division genes. Both
594 *CDKB1* and its partnering cyclins (*CYCA1*, *CYCB1*) were strongly downregulated, consistent with
595 defects in mitotic progression and multiple fission cycles (Tulin and Cross, 2014; Bisova et al.,
596 2005). The partial reduction of D-type cyclins further weakens G1/S entry, while the mild
597 repression of CDKG1 implicates misregulation of size-dependent checkpoints (Li et al., 2016;
598 Umen and Goodenough, 2001). The coupled downregulation of plastid fission genes that we found
599 through co-expression network analyses aligns with the tight synchronization between plastid
600 division and cell cycle progression in unicellular algae (Sumiya et al., 2016; Clark-Cotton et al.,
601 2025). It was shown that conditional repression of plastid genes (*rpoA*, *rps12*) that are required for
602 the expression machinery halts Chlamydomonas growth whereas cells resume proliferation once
603 chloroplast function is restored (Ramundo et al., 2013). The cell cycle in *kea1* is not arrested.
604 Instead, mutant cells progress more slowly through G1, delaying the onset of cell and chloroplast
605 division. After entry into S/M phase, cells more often exhibit specific division defects, including
606 potentially misplaced division planes and incomplete cytokinesis, which may lead to remerging
607 events. Elevated light intensity, which stimulates growth and cell division in algae (Dupuis et al.,
608 2025), was associated with an increased occurrence of enlarged cells, consistent with division
609 defects. However, we did not assess whether the frequency of defects changes under these
610 conditions.

611 In contrast to the cell cycle-coupled plastid division in Chlamydomonas, plant plastids
612 divide autonomously, controlled by developmental programs, tissue context, and land-plant-
613 specific proteins such as PDV1/2 (Okazaki et al., 2009; Vercruyssen et al., 2015). Thus, while IE
614 *KEA* loss in both systems impairs plastid function, the downstream impact is filtered through

615 fundamentally different organizational logics: cell cycle-plastid coupling in algae versus tissue-
616 specific developmental regulation in plants. However, our finding that *kea1* cells downregulate
617 plastid division and accumulate enlarged chloroplasts parallels observations in Arabidopsis, where
618 *kea1kea2* mutants harbor fewer but enlarged plastids per cell (Kunz et al., 2014; Aranda-Sicilia et
619 al., 2016). Despite differences in cellular architecture — one plastid per algal cell versus many
620 plastids per plant cell — KEA transporters thus appear broadly required to coordinate plastid
621 division and maintain organelle size.

622 At present, it remains difficult to distinguish whether the observed cell-cycle defects arise
623 directly from perturbed ion homeostasis or represent secondary consequences of reduced
624 photosynthetic performance and metabolic stress. In Chlamydomonas, cell-cycle progression is
625 tightly coupled to cellular energy status. Moreover, photoinhibition or chloroplast dysfunction is
626 likely to delay progression through G1. Thus, the enlarged cell size and delayed division observed
627 in *kea1* may reflect a combination of direct plastid signaling effects and indirect responses to
628 altered photosynthetic capacity.

629 While the present work defines key physiological consequences of *KEA1* loss, future work
630 will be required to disentangle primary ion transport defects from downstream physiological
631 consequences. In particular, compartment-resolved measurements of $K^+$ and pH, for example
632 using targeted fluorescent sensors or electrophysiological approaches, would help clarify how
633 CrKEA1 activity shapes ion homeostasis. Combining such approaches with time-resolved
634 ionomics across the diurnal cycle, and their extension to single-cell measurements, may further
635 reveal how perturbations in chloroplast ion transport propagate to whole-cell physiological
636 responses and cell-cycle dynamics.

637 **Conclusions**

638 Given that $K^+$ fluxes have universal roles in driving cell-cycle progression in microalgae
639 and beyond (Urrego et al., 2014; Feeney et al., 2016; Henslee et al., 2017; Rodríguez et al., 2024),
640 our integrated ionomics-single-cell imaging approach offers a roadmap for future studies to
641 unravel how perturbations in organellar ion transport translate into systemic defects in growth,
642 proliferation, and stress adaptation. Taken together, our results support a model in which IE KEA
643 transporters are evolutionarily conserved regulators of plastid homeostasis, linking ion transport
644 to ribosome assembly and photosynthetic capacity. Yet the downstream phenotypes diverge,

645 reflecting the distinct cellular architectures of unicellular algae and multicellular plants. *kea1*
646 mutants expose defects in cell cycle fidelity absent in plants, while Arabidopsis mutants reveal
647 developmental and signaling adjustments not observed in algae. These findings illuminate how
648 plastid ion transport serves as a deeply conserved module, whose consequences for cell physiology
649 depend on lineage-specific evolutionary trajectories.

650 **Material and Methods**

651 *Algae cultivation and growth measurements*

652 All Chlamydomonas (*Chlamydomonas reinhardtii*) *kea1* mutants and complementation lines
653 generated in this study share the CC-406 cw15 mt- background (Davies and Lyall, 1973) which
654 served as the reference ("wild type", WT) in this study.
655 Algae were grown in Tris-acetate-phosphate (TAP; Gorman and Levine, 1965) medium under
656 constant light of 25 µmol photons $m^{-2}$ $s^{-1}$ at 23°C and shaking at 125 rpm if in liquid culture, unless
657 indicated otherwise. TAP was supplemented with 1% (w/v) sorbitol for culturing strain cc406. For
658 photoautotrophic conditions algae were grown in Sueoka's high salt medium (HSM; Sueoka,
659 1960).
660 The optical density at 750 nm (OD750) of liquid cultures was determined by a UV-vis
661 spectrophotometer and the cell count $ml^{-1}$ by a BD Accuri™ C6 plus flow cytometer. To determine
662 a conversion factor to calculate the size of the cells measured from FSC-A, the flow cytometer was
663 calibrated with CS&T RUO Beads (BD Biosciences, USA). The derived linear regression was y =
664 $2.432 \times 10^6 x + 1{,}706$ with y being the diameter (µm) and x the FSC-A values.

665 *Plant growth and generation of CrKEA1-YFP plants*

666 Arabidopsis (*Arabidopsis thaliana*) plants were grown at 110 µE illumination in long-day
667 conditions (16 h/8 h at 22°C). To generate transgenic *CrKEA1* Arabidopsis plants, the codon-
668 optimized *CrKEA1* coding sequence (Cre04.g220200_4532.1, fused to a Twin-Strep tag) was
669 cloned into the binary Ti vector *pG20_TEV_mVenus_Hyg* via Golden Gate assembly downstream
670 of the UBQ10 promoter (Addgene ID #240651; Schwartz et al., 2025) as described in
671 Supplemental Table S9. Venus is referred to throughout as YFP. The resulting *CrKEA1-*
672 *TwinStrep-TEV-YFP* (short *CrKEA1-YFP*) fusion construct was used for stable transformation of
673 the Arabidopsis T-DNA insertion line *kea1-1kea2-1* (Kunz et al., 2014). The final construct was

674 transformed into Arabidopsis via the *Agrobacterium tumefaciens* (GV3101 containing *pSOUP*) by
675 the floral dip method as described previously (Clough and Bent, 1998). The $T_1$ generation was
676 selected on 25 µg/ml Hygromycin-containing 1/2 strength MS medium (Murashige and Skoog,
677 1962) and screened for phenotypical rescue of the *kea1-1kea2-1* mutant. Expression of *CrKEA1-*
678 *YFP* was verified via immunoblotting (Höhner et al., 2019).

679 *Generation of Chlamydomonas kea1 mutants by CRISPR/Cas9*

680 *kea1* mutants were created in CC-406 cw15 $mt^-$ using insertional mutagenesis by the
681 CRISPR/Cas9 technique following the protocol established (Greiner et al., 2017). Briefly, a
682 crRNA sequence was designed to target *CrKEA1* exon-19. The crRNA was annealed with
683 tracrRNA (Integrated DNA Technologies, #1072533) to generate guide RNAs (gRNA) and then
684 conjugated with Alt-R® S.p. Cas9 Nuclease V3 (Integrated DNA Technologies, #1081058) to
685 form the SpCas9/gRNA complex. The latter was co-transformed into Chlamydomonas with a
686 mutation oligonucleotide containing orientation and frameshift tolerant STOP codons and with the
687 plasmid pBC1 (pJR38, Neupert et al., 2009) conferring paromomycin resistance. Transformation
688 was carried out on a NEPA21 electroporator (Nepa Gene). Cells were selected under 10 µg $ml^{-1}$
689 paromomycin and screened by colony-PCR. Knock-out of *CrKEA1* was confirmed by
690 immunoblotting using CrKEA1 antibodies. Relevant sequences are listed in Supplemental Table
691 S1.

692 *Generation of kea1 complementation lines*

693 The *CrKEA1* gDNA sequence, including the native promoter, was inserted into *pLM161* (Cr-
694 Venus-3xFLAG; hygromycin), applying the recombineering approach described in Emrich-Mills
695 et al., 2021; Supplemental Table S10). Nuclear transformation was achieved by the glass bead
696 method (Kindle, 1990). Transformed *kea1* cells were selected under 100 µg $ml^{-1}$ hygromycin
697 followed by screening for the expression of the CrKEA1-YFP fusion protein by fluorescence
698 microscopy and immunoblot.

699 *Design of the CrKEA1 antibody*

700 To generate antibodies against CrKEA1, a DNA fragment codon optimized for *E. coli* synthesized
701 by Twist Bioscience (California, USA), was cloned into the plasmid *pHue* (Catanzariti et al., 2004;
702 modified for Gold Gate cloning) resulting in the plasmid *pHue_CrKEA1-aa94-337* (Supplemental

703 Table S11). Proteins were expressed in *E. coli* strain BL21 (DE3) overnight at 23°C and lysed in
704 lysis buffer (20 mM Tris-HCl, pH 8.0, 300 mM NaCl and 10 mM imidazole). The HisUbiquitin-
705 tagged CrKEA1 fragment was extracted by an IMAC column, the tag was cleaved by Ubiquitin
706 Specific Peptidase 2 (USP2; Baker et al., 2005) and the sample passed over a size exclusion
707 chromatography (SEC) column in SEC buffer (20 mM Tris-HCl, 300 mM NaCl). The SEC elution
708 was reapplied to an IMAC column, where the tag-less protein was recovered from the flow-
709 through. The pure protein CrKEA1-aa94-337 in 20 mM Tris pH 8, 200 mM NaCl, and 5% glycerol
710 served BioGenes (Berlin, Germany) as antigen to produce polyclonal antibodies. Serum was used
711 for immunodetection.

712 *Protein extraction and immunoblotting*

713 For Chlamydomonas, cultures grown to an OD750 of 2 were pelleted and resuspended in Laemmli
714 SDS loading dye containing 50 mM DTT. Samples set to an OD of 22 were heated to 60°C for 20
715 min and then subjected to SDS PAGE. Immunoblotting was performed on PVDF membranes with
716 secondary antibodies coupled to horse radish peroxidase and the enhanced chemiluminescence
717 (ECL) system. For Arabidopsis, immunoblotting was performed as described before (Höhner et
718 al., 2019). The following antibodies were used: GFP (Roche 11814460001), NAB1 (Agrisera
719 AS08 333), AtKEA1 (Bölter et al., 2020), CrKEA1 (this study)

720 *Element determination via TXRF*

721 Cultures for element analysis were washed thrice in isotonic buffer (300 mM sorbitol, 20 mM
722 HEPES pH 7.5, 5 mM EDTA, 10 mM $NaHCO_3$). Cell numbers in washed samples were
723 individually determined for each sample using a Neubauer Improved counting chamber (Hecht-
724 Assistent, Sondheim vor der Rhön, Germany). Elemental analysis was performed by total
725 reflection X-ray fluorescence (TXRF) using an S4 T-STAR (Bruker, Berlin, Germany) as
726 described in Holzner et al., 2026. The sample was mixed in a 1:1 ratio with internal standards to
727 final concentrations of 1 ppm vanadium (W-L) and 1 ppm gallium (Mo-K) and 0.1% (w/v)
728 polyvinyl alcohol (PVA). Samples were applied to silicon-coated quartz glass carriers and
729 measured at 50 kV for 1000 s per sample using Mo-K and W-L excitation. To determine
730 background element levels, a sample of isotonic buffer was measured, which was subtracted from
731 the respective samples. Element concentrations were normalized to the cell number of each

732 sample. Where indicated, values were additionally normalized to the average cell volume as
733 determined by flow cytometry (FC).

734 *Determination of cytosolic pH*

735 Cytosolic pH was determined using the ratiometric fluorescent dye BCECF-AM, based on the
736 approach described previously (Pang et al., 2023). Cells were harvested and resuspended to ~2 ×
737 $10^7$ cells $ml^{-1}$ in NMG buffer (10 mM HEPES, 60 mM KCl, 3 mM $MgCl_2$, pH 6.8). BCECF-AM
738 was added to a final concentration of 5 µM, and cells were incubated for 1 h at 36 °C to allow dye
739 uptake and intracellular ester cleavage. Cells were then washed and resuspended in medium to
740 remove extracellular dye. Fluorescence measurements were performed with a Spark plate reader
741 (TECAN, Switzerland) in 96-well plates using excitation wavelengths of 440 ± 10 nm and 490 ±
742 10 nm and emission detection at 535 ± 10 nm. Dye uptake and localization were verified with
743 confocal imaging (Stellaris 5, Leica, Wetzlar). BCECF fluorescence was excited at 448 nm and
744 emission was detected at 530 ± 10 nm.
745 For calibration, TAP was substituted with NMG buffer (10 mM HEPES, 60 mM KCl, 3 mM
746 $MgCl_2$, pH 6.8). BCECF-loaded cells were equilibrated with NMG buffers of defined pH (4–9)
747 containing 100 µM nigericin to equilibrate intra- and extracellular pH. The resulting titration curve
748 (average of three replicates) was used to convert fluorescence ratios (490/440 nm) to cytosolic pH
749 values.

750 *Pulse-Amplitude-Modulation (PAM) fluorometry and leaf area*

751 IMAGING-PAM systems (M-Series Maxi and Hexagon; Walz GmbH, Effeltrich, Germany) were
752 used for leaf area and PAM measurements. For Arabidopsis, experiments were performed as
753 described previously (Schneider et al., 2019). For Chlamydomonas drop cultures, spotted cultures
754 were cultivated under standard conditions for 3 days before subjecting them to PAM
755 measurements. For liquid culture, cells grown in 50 ml were adjusted to an OD of 1.5, and equal
756 volumes (2 ml) were transferred into multi-well plates for PAM measurements after 15 min dark
757 adaptation. For NPQ induction and photoinhibition (PI) experiments, cultures were adjusted to
758 $OD_{750} \approx 0.12$ and transferred to 10 ml beakers that were continuously stirred during measurements.
759 NPQ induction was measured under actinic light (646 PAR) following standard PAM protocols.
760 For photoinhibition experiments, cultures were exposed to actinic high light (646 PAR) and
761 recovery of PSII efficiency was monitored over time. During recovery, samples were incubated

762 for 20 min under low light (15 µmol photons $m^{-2}$ $s^{-1}$), followed by 10 min dark adaptation before
763 determination of $F_v/F_m$. This cycle was repeated for 5 h. Lincomycin was added to one set of
764 samples after the first post-illumination $F_v/F_m$ measurement to inhibit chloroplast protein
765 synthesis.

766 *Protoplast isolation and localization of CrKEA1-YFP in Arabidopsis and Chlamydomonas*

767 Protoplasts were isolated from Arabidopsis leaves as described before (Wu et al., 2009).
768 Localization of CrKEA1–YFP in Arabidopsis protoplasts and intact Chlamydomonas cells was
769 performed using a Stellaris 5 confocal laser scanning microscope (Leica, Wetzlar, Germany),
770 equipped with a 405 nm diode laser, a supercontinuum white light laser (WLL), and a Power
771 Hybrid (HyD S) detector. Chlorophyll autofluorescence was excited at 405 nm and detected
772 between 620 and 810 nm, while YFP was excited at 515 nm and detected between 520 and 580
773 nm.

774 *Transmission Electron Microscopy*

775 Sample preparation was performed as previously described (Lübben et al., 2024). Chlamydomonas
776 samples were frozen under high pressure (2,100 bar) in culture medium using an EM HPM100
777 (Leica Microsystems, Germany). Following cryofixation, samples underwent freeze substitution
778 (Peschke et al., 2013; Walther and Ziegler, 2002) in an EM AFS2 system (Leica Microsystems),
779 after which they were embedded in Epon 812 and polymerized for 16 h at 63 °C. Ultrathin sections
780 of 50 nm (ultra 35°, 3.0 mm, DiATOME) were cut on an Ultracut E ultramicrotome (Leica
781 Microsystems) and collected on collodion-coated, 400-mesh copper grids (Science Services
782 GmbH, Germany). Prior to imaging, sections were post-stained with lead citrate (Reynolds, 1963).
783 Samples were examined in a Zeiss EM 912 transmission electron microscope (Zeiss, Germany)
784 equipped with an integrated OMEGA energy filter operated in zero-loss mode at 80 kV. Images
785 were captured at a nominal magnification of 12,500× using a 2k×2k slow-scan CCD camera
786 (Tröndle Restlichtverstärkersystem, Germany).

787 *Whole Genome Sequencing*

788 gDNA was isolated according to Dutcher et al., 2012 and sent to BMKGene (Biomarker
789 Technologies, Münster, Germany / Hongkong) for Illumina sequencing. CLC Genomics

790 Workbench and Integrative Genomics Viewer (IGV) was used to confirm stop codon insertion in
791 exon 19. TDNAscan (Sun et al., 2019) was used to search for additional off-target insertions.

792 *RNA-seq after ribo-depletion, Gene Ontology analysis, and constructing co-expression networks*

793 Four replicates per genotype and condition were sampled to obtain RNA-seq from the light shift
794 experiment. RNA was extracted using TRIzol™ reagent (Ambion, USA; Simms et al., 1993)
795 following the manufacturer's instructions. RNA was further purified and DNA contaminations
796 were removed using the Monarch® RNA Cleanup Kit (NEB) according to the manufacturer's
797 protocol. RNA quality control, depletion of ribosomal RNA, library preparation, and eukaryotic
798 lncRNA Sequencing was performed by BMKGene on an Illumina platform, generating over 10
799 Mio paired-end reads (150 bp) per sample. RNA-seq data were analyzed on the Galaxy platform
800 (usegalaxy.eu; Galaxy-Community, 2024) using the tools, reference genome and annotation file
801 (JGI Phytozome) listed in Supplemental Table S12. For statistical analysis and assessment of
802 differentially expressed genes (DEGs), the low read count filters were set to "1-count-per-million"
803 (CPM=1) in at least 3 samples. DEGs were considered significant with an adjusted p-value $< 0.05$.
804 Gene Ontology (GO) term enrichment was assessed with g:Profiler (Kolberg et al., 2023) and
805 condensed with REVIGO (Supek et al., 2011). Co-expression networks were calculated using the
806 StreptoNet (https://rshiny.gwdg.de/apps/streptonet/) framework (Dadras et al., 2023) and
807 constructed based on gene lists of interest. Chlamydomonas genes were annotated using the best
808 BLAST hits against Arabidopsis genes. CoNekT (https://conekt.sbs.ntu.edu.sg/) framework was
809 used to compare clusters of co-expression networks. See Supplemental Table S12 for further
810 details.

811 *RNAseq with focus on ribosomal RNA (MiSeq NGS)*

812 To analyze plastid rRNA processing, RNA was extracted from cells grown in HSM under
813 moderate light (100 µmol $m^{-2}$ $s^{-1}$) as mentioned above. Library preparation was performed using
814 the NEBNext® Ultra™ II RNA Library Prep Kit (NEB). RNA and library quality were assessed
815 using the Agilent 2100 Bioanalyzer. Next-generation sequencing (2 × 300 paired-end) was carried
816 out on a MiSeq sequencer (Illumina, San Diego, CA, USA), generating over 1.5 million paired-
817 end reads per sample with a length of 200-250 nt. Data processing was performed on usegalaxy.eu
818 (Galaxy-Community, 2024) as described above. The effective genome size (113,516,734 bp) was
819 determined by subtracting the total number of ambiguous (N) bases (1,114,981 bp) from the actual

820 Chlamydomonas genome size (114,631,715 bp). To analyze coverage differences between
821 samples, mapped reads were processed through the BamCoverage and BamCompare pipelines of
822 the deepTools suite (Ramírez et al., 2016), focusing on plastome rRNA transcripts. BigWig output
823 files generated from both tools were exported as bedGraph (.csv format).

824 *Non-Radioactive RNA blots*

825 RNA blots were performed using 3'-Digoxigenin (DIG)-labeled DNA probes from metabion
826 international AG, Germany (Supplemental Table S13; Holtke & Kessler 1990; Ramkissoon et al.,
827 2006). RNA samples were denatured at 55°C for 45 minutes in denaturing buffer (15% (v/v)
828 DMSO, 7% (w/v) Glyoxal in 20 mM MOPS, 5 mM sodium acetate, 1 mM EDTA, pH 7) before
829 adding loading dye. Samples were separated on a 1.2% agarose MOPS gel at 4°C, and transferred
830 onto a nylon membrane via capillary blotting in 20x SSC (3M NaCl, 0.3M Trisodium Citrate
831 dihydrate, pH 7) overnight, followed by UV crosslinking. To develop the blot, the DIG Northern
832 Starter Kit (Roche, Cat. No. 12 039 672 910) was utilized as described by the manufacturer but
833 using 50°C for hybridisation.

834 *Single-cell time-lapse imaging and image analysis*

835 The microchannel layout was based on the original *Mother Machine* design for bacterial single-
836 cell studies (Wang et al., 2010) and was modified to enable the observation of Chlamydomonas
837 under hydrogel-mediated confinement. Hydrogel patterning was carried out using the
838 photolithographic microfabrication workflow previously described for PEG-based hydrogels
839 (Stöberl et al., 2023), with adjustments to the precursor composition and pattern geometry. Flow
840 channels were filled with diluted cultures ($5 \times 10^4$ cells $mL^{-1}$) and placed in a stage-top chamber
841 (okolab, H101-CRYO-BL) connected to a cryostatic water bath (Lauda, RE415S). The medium
842 temperature was adjusted to 23°C and flow rate to 200 µl $h^{-1}$. Cells were continuously illuminated
843 with 25 µE. Images were acquired every 5 min on a Leica DMi8 Thunder microscope (Leica,
844 Wetzlar) using LASX. Chlorophyll autofluorescence was excited with a Leica LED8 at 475 nm
845 and detected with a Leica DFC9000 GTC camera with a 642/80 filter. Image analysis was
846 conducted in Cell-ACDC (Padovani et al., 2022). A custom-trained Cellpose (Pachitariu and
847 Stringer, 2022) model was used to segment cells. Segmentation was controlled and corrected in
848 the Cell-ACDC GUI. Segmented objects were then tracked with Trackastra (Gallusser and
849 Weigert, 2025) with the general_2d model using the chlorophyll autofluorescence channel as

input. Truthful tracking was checked in the Cell-ACDC GUI. Out-of-focus cells, division failures and cells with an unobservable future were manually marked in the Cell-ACDC GUI for filtering in downstream analysis. Resulting .csv files were filtered and analysed in a custom phyton script.

*Sequence alignment, structure prediction, and domain annotations*

Multiple Sequence alignment was performed by the *MultAlin* online tool (Corpet 1988). Structural models were predicted using AlphaFold3 (DeepMind; Abramson et al., 2024). The default parameters were used, and no experimental structural constraints were applied. For model visualization, we used UCSF ChimeraX (Pettersen et al., 2021). For domain annotations, information obtained from Uniprot.org (Q9ZTZ7) and AlphaFold3 prediction was combined.

*Accession numbers and annotations*

Chlamydomonas strains CC-406 cw15 $mt^-$, CC-4533 cw15 $mt^-$, the CLiP line (Li et al., 2016) LMJ.RY0402.187220, and the BAC (well number 19-B-5) encoding the *CrKEA1* (Cre04.g220200_4532.1) gDNA were obtained from the Chlamydomonas Resource Center (University of Minnesota, USA). The strains *kea1* and *CrKEA1-YFP* (in *kea1*), generated in this study, are available as CC-6360 kea1-1 $mt^-$ and CC-6361 kea1-1_CrKEA1-YFP $mt^-$, respectively. The Arabidopsis T-DNA insertion mutant *kea1-1kea2-1* (SAIL_586_D02, SALK_045324) (Kunz et al., 2014) is available in the stock centers: ABRC: CS72318 or NASC: N72318. All other GeneIDs are listed in the Supplemental Table S14 and S15. RNA-seq data generated in this study have been deposited in the NCBI Sequence Read Archive (SRA) under BioProject accession number PRJNA1343327 (Wunder et al., 2025).

870 **Supplemental Data**

871 Supplemental Figure S1: Alignment of inner envelope (IE) KEA protein sequences from
872 Chlamydomonas and Arabidopsis.
873
874 Supplemental Figure S2: Generation of the CrKEA1 antibody and testing the CLiP line.
875
876 Supplemental Figure S3: Genomic characterization of the kea1 CRISPR/Cas9 knock-out site and
877 immunoblotting.
878
879 Supplemental Figure S4: Genomic characterization of the *kea1* CRISPR/Cas9 knock-out site
880 (part2).
881
882 Supplemental Figure S5: Characterization of independent *CrKEA1–YFP* (*kea1*) complementation
883 lines.
884
885 Supplemental Figure S6: CrKEA1-YFP localizes to the plasdtid envelope.
886
887 Supplemental Figure S7: Confocal microscopy of chloroplast morphology and ultrastructural
888 analysis of kea1 cells.
889
890 Supplemental Figure S8: Ionomic profiles expressed per cell and calibration of cytosolic pH
891 measurements in Chlamydomonas kea1 and control strains.
892
893 Supplemental Figure S9: Scatter plots corresponding to the flow cytometry experiment shown in
894 Figure 3.
895
896 Supplemental Figure S10: Additional results related to the RNA-seq experiment.
897
898 Supplemental Figure S11: Comparison of plastid rRNA processing pathways in Chlamydomonas
899 and Arabidopsis.
900
901 Supplemental Figure S12: rRNA-seq analysis of plastid rRNA processing including the *CrKEA1-*
902 *YFP* complementation line.
903
904 Supplemental Figure S13: RNA blot analysis of plastid rRNA processing in the *kea1* mutant.
905
906 Supplemental Figure S14: Structural comparison of AtKEA1 and CrKEA1.
907
908 Supplemental Figure S15: Characterization of the Arabidopsis *kea1kea2* line complemented with
909 *CrKEA1-YFP*.

910
911 Supplemental Figure S16: Single cell live imaging of *kea1* and WT.
912
913 Supplemental Tables
914
915 Supplemental References

916 **Acknowledgements**

917 At LMU, we thank Berina Isakovic and Yuling Ma for help in isolating *kea1* mutant and
918 complementation lines, Andreas Brachmann for supervising the rRNA seq experiment, and
919 Nikolay Kayo Manavski and Jörg Meurer for teaching RNA work, Stefan Stöberl and Bettina
920 Bölter for discussions about hydrogel flow cell chips and result interpretations, respectively.
921 Lastly, we thank Alexander Schober from NTU Singapore for providing the Goldengate
922 compatible pHue vector.
923

924 **Funding**

925 H.-H.K., T.W., S.M., and L.J.H. were funded by the Deutsche Forschungsgemeinschaft (DFG)
926 SFB-TR 175, project B09, and J.N. and M.O. by SFB-TR 175, project A06. J.d.V.
927 acknowledges funding by the DFG within the framework of MAdLand (SPP 2237), in which
928 Z.M.A. is a PhD student (project 440231723). P.G. was supported by DFG project number
929 456013262. L.C.M.M. was supported by BBSRC-NSF/BIO (BB/Y000323/1) and UKRI-
930 Future Leaders Fellowship (MR/T020679/1 and MR/Y034074/1). Confocal microscopy work
931 was funded by DFG (INST 86/2231-1 FUGG) and (SFB-TR 175, project Z01) to H.-H.K..
932 K.M.S. was funded by the European Union (ERC, MITOSIZE, 101169998). Views and
933 opinions expressed are, however, those of the author(s) only and do not necessarily reflect
934 those of the European Union or the European Research Council. Neither the European Union
935 nor the granting authority can be held responsible for them.

936 **Figures and Legends**

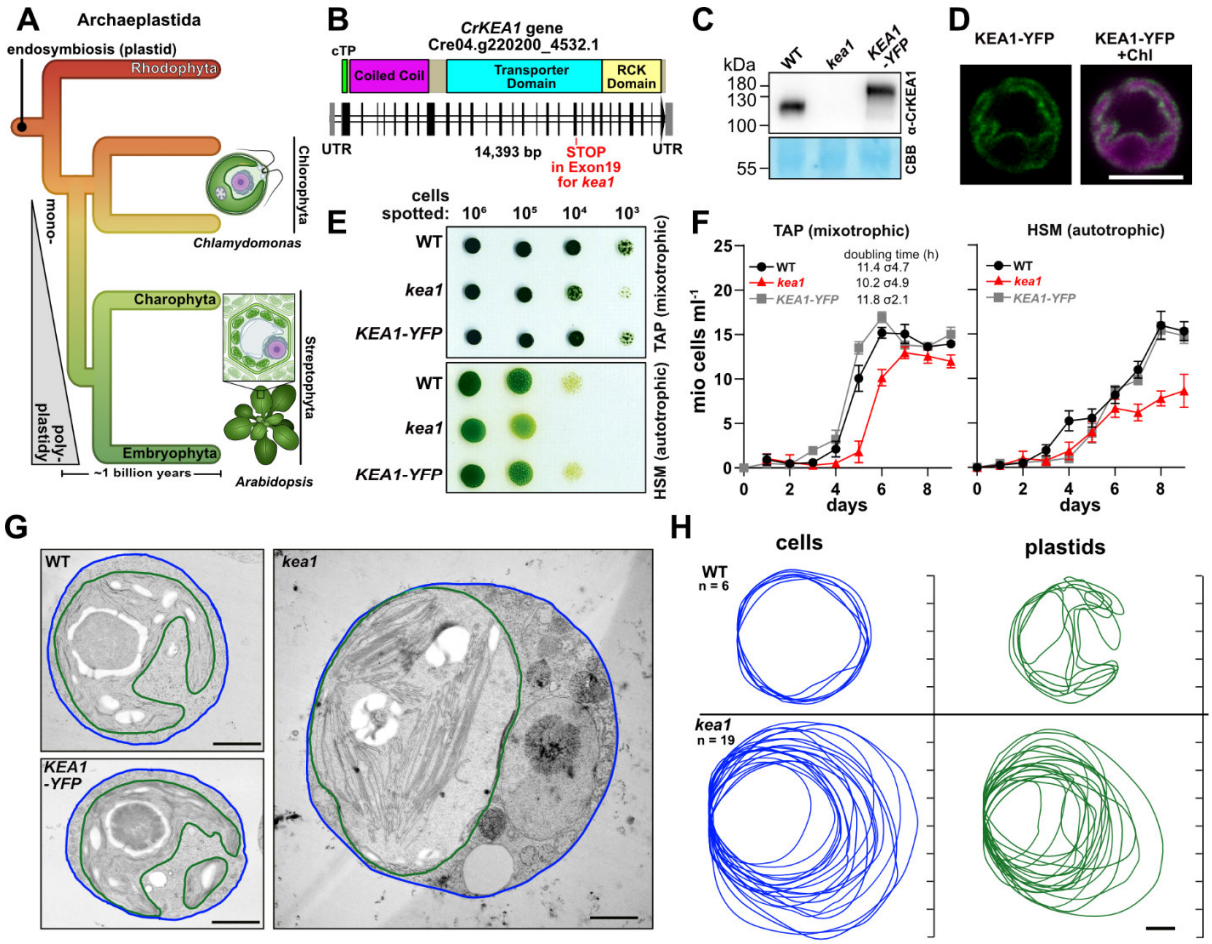


937
938 **Figure 1: Characterization of *CrKEA1* knock-out and complementation lines: growth, localization,**
939 **and cellular ultrastructure. (A)** Simplified cladogram of the Archaeplastida showing the phylogenetic
940 relationship between monoplastidic *Chlamydomonas* algae and multicellular, polyplastidic *Arabidopsis*
941 plants, both derived from a common monoplastidic ancestor that diverged approximately 1 billion years
942 ago. **(B)** Schematic of the CRISPR/Cas9 knock-out line *kea1*. **(C)** Immunoblot using anti-CrKEA1
943 antibodies on total protein extracts from WT, *kea1*, and the complementation line (*CrKEA1–YFP* expressed
944 in *kea1*). **(D)** Localization of YFP-tagged CrKEA1 to the plastid envelope in the complementation line.
945 Scale bar 5 µm. **(E)** Drop cultures grown on mixotrophic (acetate-containing TAP) and photoautotrophic
946 (HSM) solid media at 25 µE. **(F)** Growth curves of mixotrophic and photoautotrophic liquid cultures at 25
947 µE. Cell counts are shown as mean ± SD (n = 3), and calculated doubling times are indicated as mean ± SD
948 (σ). **(G)** Representative TEM images of cells grown in HSM at 100 µE. Scale bar 1 µm. **(H)** Comparison
949 of cell and chloroplast size and shape based on TEM micrographs shown in panel G. Scale bar 1 µm.
950

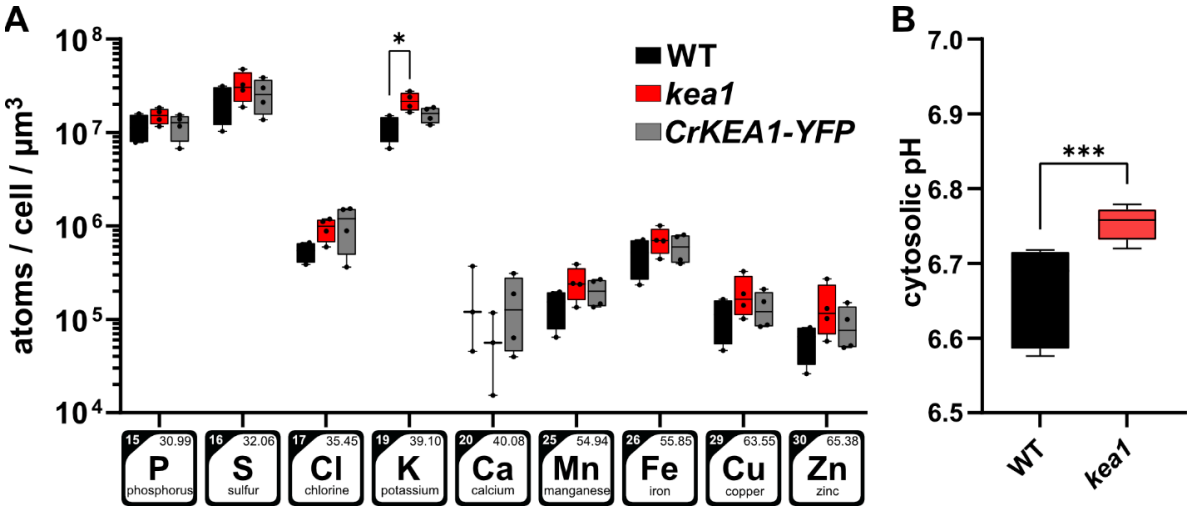


**Figure 2. Cellular ion composition and cytosolic pH in *kea1*. (A)** Volume-normalized ionomic profiles determined by Total Reflection X-Ray Fluorescence (TXRF). Whole-cell elemental composition was normalized to the average cell volume derived from flow cytometry measurements. Data were evaluated by one-way ANOVA for each element separately, followed by Tukey's multiple comparison test. n = 4 **(B)** Cytosolic pH determined using the ratiometric fluorescent dye BCECF-AM. Fluorescence ratios were measured and converted to cytosolic pH values using a calibration curve generated with nigericin in buffers of defined pH. Statistical analysis was performed using unpaired t test; n = 9. Box plots show the median (center line), the 25th–75th percentiles (box), and the minimum and maximum values (whiskers). Asterisks indicate significant differences (* $p < 0.05$, *** $p < 0.001$). Cultures were grown in TAP at 25 µE prior to both measurements.

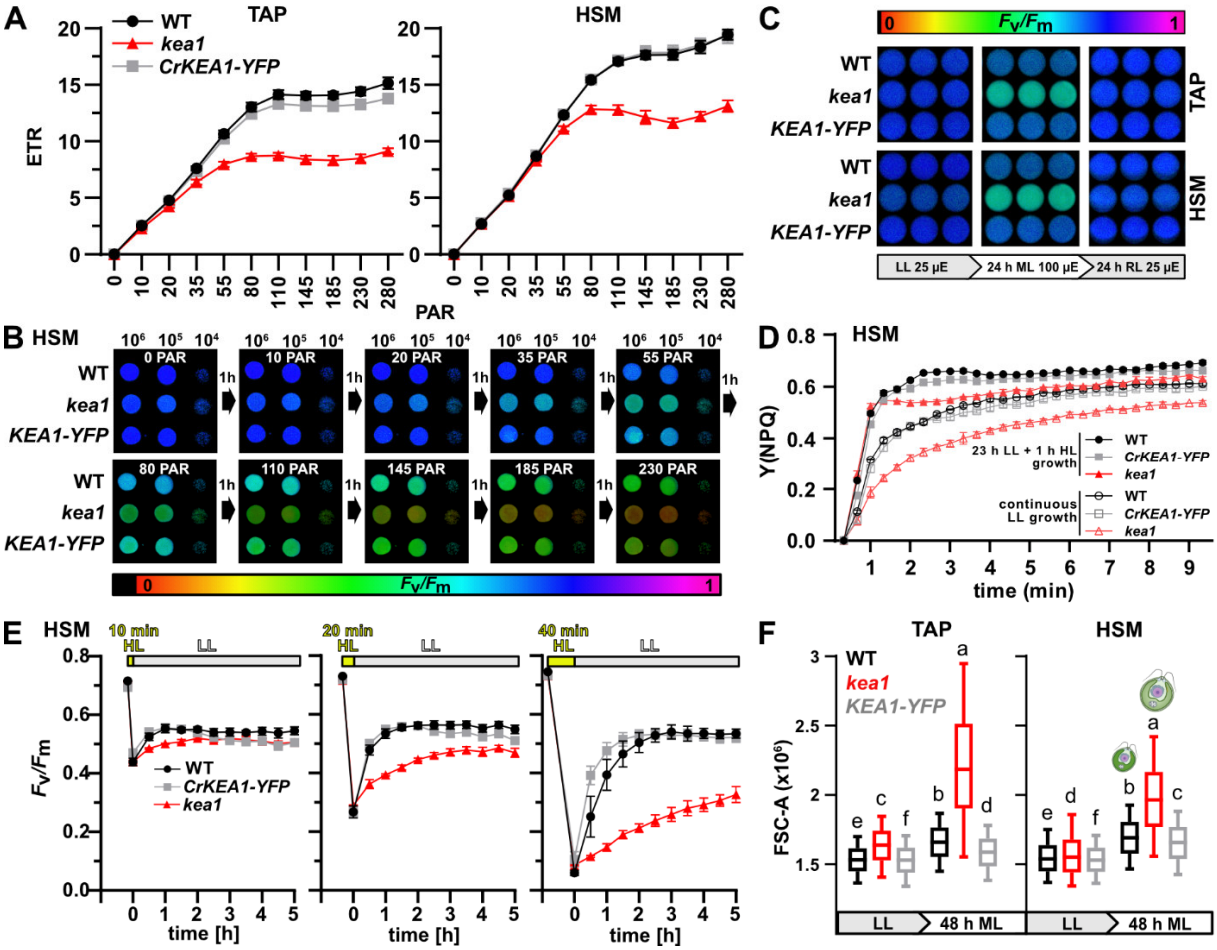


**Figure 3: Photosynthetic characterization and cell size of *kea1*. (A)** To assess the photosynthetic performance of *kea1*, liquid TAP and HSM cultures were exposed to gradually increasing light intensities, with PAR raised in 20-s intervals. Mean electron transfer rate (ETR) was plotted with standard deviation. n=4. **(B)** $F_v/F_m$ values were determined from HSM drop cultures every 1 h while stepwise increasing light intensity. **(C)** Light-shift experiment with TAP and HSM liquid cultures. $F_v/F_m$ was measured before and after transferring cultures from low light (LL) to moderate light (ML) for 24 h and back to low light for 24 h of recovery (RL). **(D)** Non-photochemical quenching (NPQ) induction at 646 PAR measured by PAM fluorometry. Cultures were either analyzed directly after growth in low light (LL, 25 µE) or growth under a light regime including a brief high-light (1h, 300 µE) treatment applied 15 h before measurements to induce LHCSR3 expression. Data represent mean values with standard deviation, n = 3. **(E)** Recovery from photoinhibition. Cultures were exposed to high-light treatments (646 PAR) for 10, 20, or 40 min to induce photoinhibition, followed by transfer to low light. Recovery of PSII efficiency was monitored as $F_v/F_m$ over time. Data represent mean values ± SD, n = 3. **(F)** The average cell size of *kea1* increased under moderate light (100 µE). Chlamydomonas cultures grown in HSM or TAP at 25 µE were shifted to 100 µE and analyzed by flow cytometry (FC) before and 48 h after the light shift. FSC-A values correlate with cell size. Boxes represent the interquartile range, the line indicates the median, and whiskers extend to the 10th and 90th percentiles; outliers (0–10 % and 90–100 %) are not shown. Letters indicate statistical groups. Statistical analysis was performed using Kruskal–Wallis test with Dunn's post hoc test. Three replicates, each containing >100,000 cells, were combined for analysis and visualization. All strains were pre-cultured at 25 µE and 23 °C in TAP under shaking conditions.

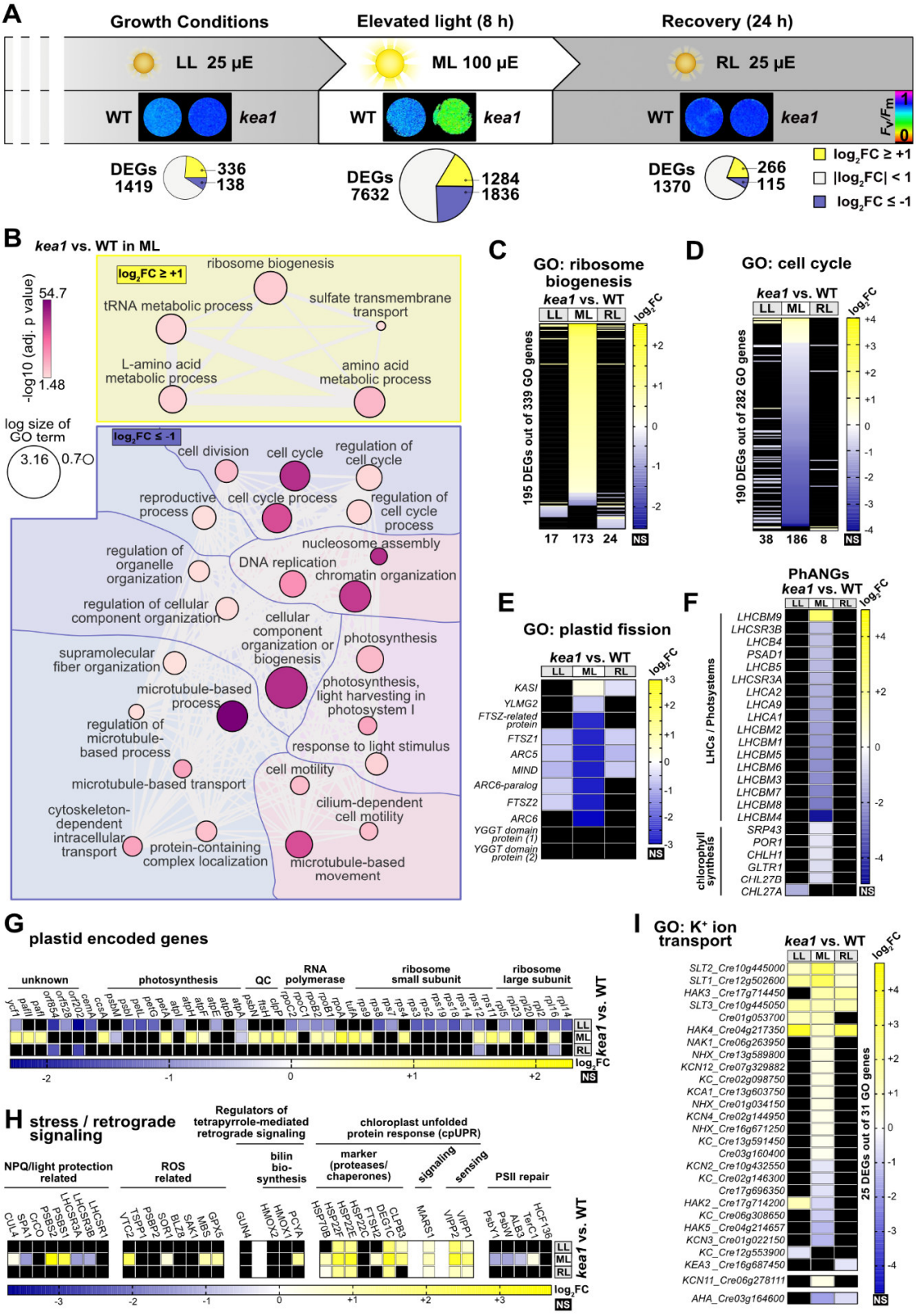
A
Growth Conditions
Elevated light (8 h)
Recovery (24 h)
LL 25 µE
ML 100 µE
RL 25 µE
WT
kea1
Fv/Fm
DEGs 1419
336
138
DEGs 7632
1284
1836
DEGs 1370
266
115
log2FC ≥ +1
|log2FC| < 1
log2FC ≤ -1
B
kea1 vs. WT in ML
-log10 (adj. p value)
54.7
1.48
log size of GO term
3.16
0.7
log2FC ≥ +1
ribosome biogenesis
tRNA metabolic process
sulfate transmembrane transport
L-amino acid metabolic process
amino acid metabolic process
log2FC ≤ -1
cell division
cell cycle
regulation of cell cycle
reproductive process
cell cycle process
regulation of cell cycle process
nucleosome assembly
regulation of organelle organization
DNA replication
chromatin organization
regulation of cellular component organization
cellular component organization or biogenesis
photosynthesis
supramolecular fiber organization
microtubule-based process
photosynthesis, light harvesting in photosystem I
regulation of microtubule-based process
response to light stimulus
cell motility
microtubule-based transport
cilium-dependent cell motility
cytoskeleton-dependent intracellular transport
protein-containing complex localization
microtubule-based movement
C
GO: ribosome biogenesis
kea1 vs. WT
LL
ML
RL
log2FC
195 DEGs out of 339 GO genes
17
173
24
NS
D
GO: cell cycle
kea1 vs. WT
190 DEGs out of 282 GO genes
38
186
8
NS
E
GO: plastid fission
kea1 vs. WT
KASI
YLMG2
FTSZ-related protein
FTSZ1
ARC5
MIND
ARC6-paralog
FTSZ2
ARC6
YGGT domain protein (1)
YGGT domain protein (2)
NS
F
PhANGs
kea1 vs. WT
LHCs / Photosystems
chlorophyll synthesis
LHCBM9
LHCSR3B
LHCB4
PSAD1
LHCB5
LHCSR3A
LHCA2
LHCA9
LHCA1
LHCBM2
LHCBM1
LHCBM5
LHCBM6
LHCBM3
LHCBM7
LHCBM8
LHCBM4
SRP43
POR1
CHLH1
GLTR1
CHL27B
CHL27A
NS
G
plastid encoded genes
unknown
photosynthesis
QC
RNA polymerase
ribosome small subunit
ribosome large subunit
kea1 vs. WT
LL
ML
RL
log2FC
NS
H
stress / retrograde signaling
Regulators of tetrapyrrole-mediated retrograde signaling
chloroplast unfolded protein response (cpUPR)
NPQ/light protection related
ROS related
bilin bio-synthesis
marker (proteases/ chaperones)
signaling
sensing
PSII repair
kea1 vs. WT
LL
ML
RL
log2FC
NS
I
GO: K+ ion transport
kea1 vs. WT
LL
ML
RL
log2FC
25 DEGs out of 31 GO genes
SLT2_Cre10g445000
SLT1_Cre12g502600
HAK3_Cre17g714450
SLT3_Cre10g445050
Cre01g053700
HAK4_Cre04g217350
NAK1_Cre06g263950
NHX_Cre13g589800
KCN12_Cre07g329882
KC_Cre02g098750
KCA1_Cre13g603750
NHX_Cre01g034150
KCN4_Cre02g144950
NHX_Cre16g671250
KC_Cre13g591450
Cre03g160400
KCN2_Cre10g432550
KC_Cre02g146300
Cre17g696350
HAK2_Cre17g714200
KC_Cre06g308650
HAK5_Cre04g214657
KCN3_Cre01g022150
KC_Cre12g553900
KEA3_Cre16g687450
KCN11_Cre06g278111
AHA_Cre03g164600
NS

983

984 **Figure 4: RNA-seq analysis of a light-shift experiment comparing transcriptional responses of *kea1***
985 **and WT. (A)** Experimental setup for the RNA-seq analysis, including $F_v/F_m$ values of the cultures and
986 pie charts indicating the number of significantly differentially expressed genes (DEGs; adj.
987 p-value < 0.05) per steady-state comparison (*kea1* vs. WT). Yellow and blue sectors denote up- and
988 downregulated genes with $|\log_2 FC| \geq 1$, respectively. n = 4. **(B)** Gene Ontology (GO) terms of the
989 *Biological Process* domain enriched among DEGs as interactive graph (REVIGO). **(C–I)** Heatmaps
990 showing $\log_2 FC$ values (*kea1* vs. WT) of significant DEGs (adj. p-value < 0.05) associated with selected
991 GO terms or gene lists. Transcripts not reaching statistical significance in a given condition are shown in
992 black (not significant, NS). "GO genes" indicates the number of genes associated with each respective
993 GO term. (C) Ribosome biogenesis (GO:0042254). (D) Cell cycle (GO:0007049). (E) Plastid fission
994 (GO:0043572). (F) Photosynthesis-associated nuclear genes (PhANGs). (G) Plastid-encoded genes. (H)
995 Selected transcripts related to stress/retrograde signaling. (I) Ion transport (including GO:0006813,
996 potassium ion transport). NHX, sodium–hydrogen exchangers; SLT, sodium/sulfate co-transporters;
997 KC(N), $K^+$ channels; HAK, high-affinity $K^+$ transporters; NAK, $Na^+$– $K^+$ pumps; AHA, plasma
998 membrane proton pumps. Gene IDs corresponding to the gene names displayed are listed in the
999 supplementary data.

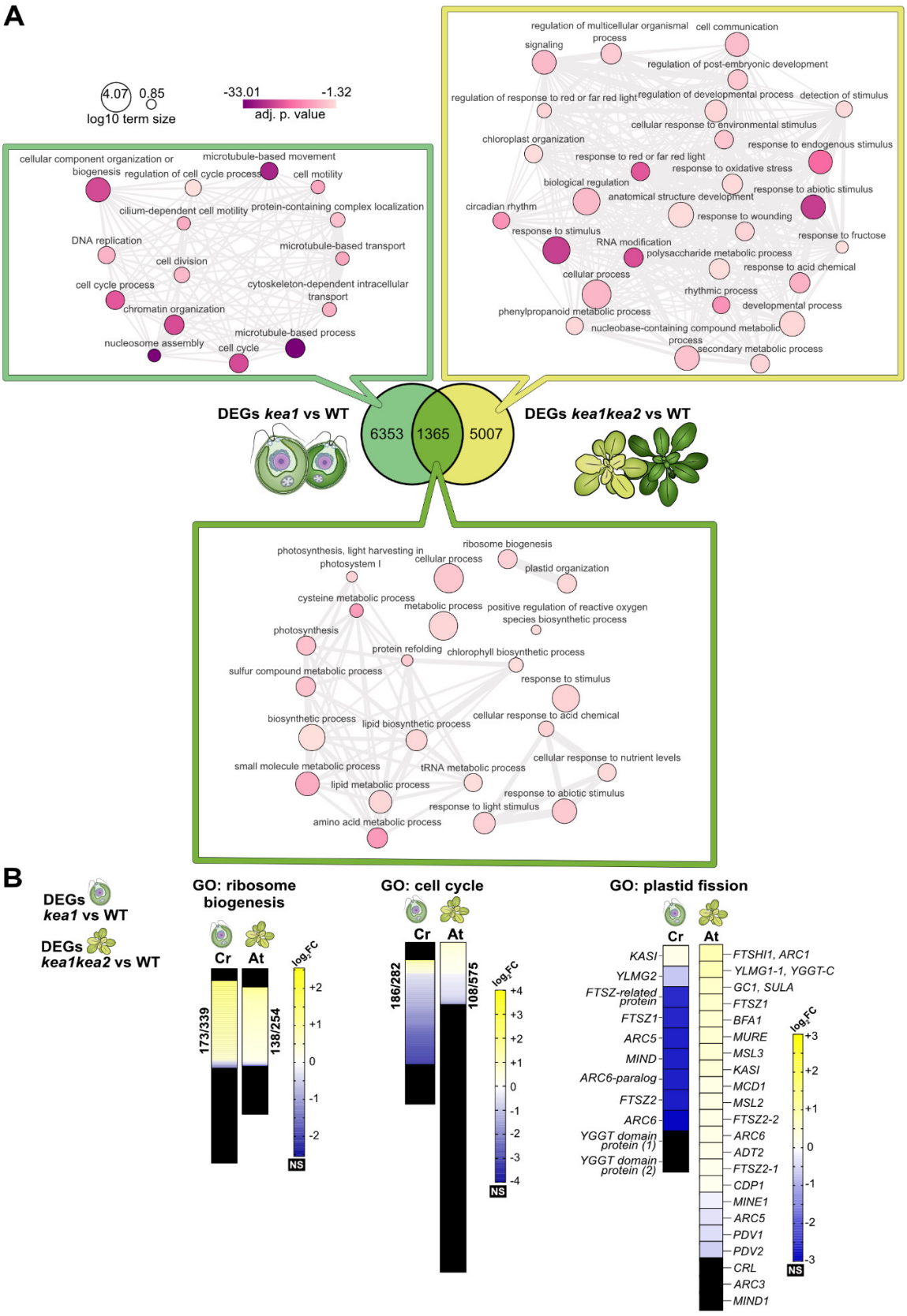
A
4.07
0.85
log10 term size
-33.01
-1.32
adj. p. value
cellular component organization or biogenesis
microtubule-based movement
regulation of cell cycle process
cell motility
cilium-dependent cell motility
protein-containing complex localization
DNA replication
microtubule-based transport
cell division
cell cycle process
cytoskeleton-dependent intracellular transport
chromatin organization
microtubule-based process
nucleosome assembly
cell cycle
regulation of multicellular organismal process
cell communication
signaling
regulation of post-embryonic development
regulation of response to red or far red light
regulation of developmental process
detection of stimulus
cellular response to environmental stimulus
chloroplast organization
response to endogenous stimulus
response to red or far red light
response to oxidative stress
biological regulation
response to abiotic stimulus
anatomical structure development
circadian rhythm
response to wounding
response to stimulus
response to fructose
RNA modification
polysaccharide metabolic process
cellular process
response to acid chemical
rhythmic process
developmental process
phenylpropanoid metabolic process
nucleobase-containing compound metabolic process
secondary metabolic process
DEGs kea1 vs WT
6353
1365
5007
DEGs kea1kea2 vs WT
photosynthesis, light harvesting in photosystem I
ribosome biogenesis
cellular process
plastid organization
cysteine metabolic process
metabolic process
positive regulation of reactive oxygen species biosynthetic process
photosynthesis
protein refolding
chlorophyll biosynthetic process
sulfur compound metabolic process
response to stimulus
biosynthetic process
lipid biosynthetic process
cellular response to acid chemical
cellular response to nutrient levels
small molecule metabolic process
tRNA metabolic process
lipid metabolic process
response to abiotic stimulus
response to light stimulus
amino acid metabolic process
B
DEGs kea1 vs WT
DEGs kea1kea2 vs WT
GO: ribosome biogenesis
Cr
At
173/339
138/254
log2FC
+2
+1
0
-1
-2
NS
GO: cell cycle
Cr
At
186/282
108/575
log2FC
+4
+3
+2
+1
0
-1
-2
-3
-4
NS
GO: plastid fission
Cr
At
KASI
YLMG2
FTSZ-related protein
FTSZ1
ARC5
MIND
ARC6-paralog
FTSZ2
ARC6
YGGT domain protein (1)
YGGT domain protein (2)
FTSHI1, ARC1
YLMG1-1, YGGT-C
GC1, SULA
FTSZ1
BFA1
MURE
MSL3
KASI
MCD1
MSL2
FTSZ2-2
ARC6
ADT2
FTSZ2-1
CDP1
MINE1
ARC5
PDV1
PDV2
CRL
ARC3
MIND1
log2FC
+3
+2
+1
0
-1
-2
-3
NS

1000

1001 **Figure 5: Cross-species transcriptomic comparison of inner envelope *KEA* mutants in**
1002 **Chlamydomonas and Arabidopsis**. **(A)** Mutants lacking inner envelope *KEA* transporters
1003 (Chlamydomonas *kea1* and Arabidopsis *kea1kea2*) in both Chlamydomonas and Arabidopsis share a subset
1004 of DEGs. Shared DEGs were identified by mapping Chlamydomonas genes to Arabidopsis orthologs using
1005 g:Orth. Significant DEGs (adj. p-value < 0.05; numbers shown in the Venn diagram) were filtered using
1006 $|\log_2 FC| \geq 0.75$ and subjected to Gene Ontology (GO) enrichment analysis with g:Profiler (*Biological*
1007 *Process* domain). GO terms are shown as interactive graph (REVIGO). Chlamydomonas DEGs correspond
1008 to the moderate light (ML) condition. Shared DEGs are enriched for *ribosome biogenesis* (GO:0042254),
1009 whereas enrichment for *cell cycle* (GO:0007049) is observed only in Chlamydomonas. **(B)** Heatmaps
1010 display $\log_2 FC$ values for all genes annotated to *ribosome biogenesis*. Only significant DEGs (adj.
1011 p-value < 0.05) are color-coded, while non-significant (NS) or undetected genes are shown in black.
1012 Numbers indicate the count of significant DEGs relative to the total number of genes annotated to the
1013 respective GO term (DEGs / GO term size).

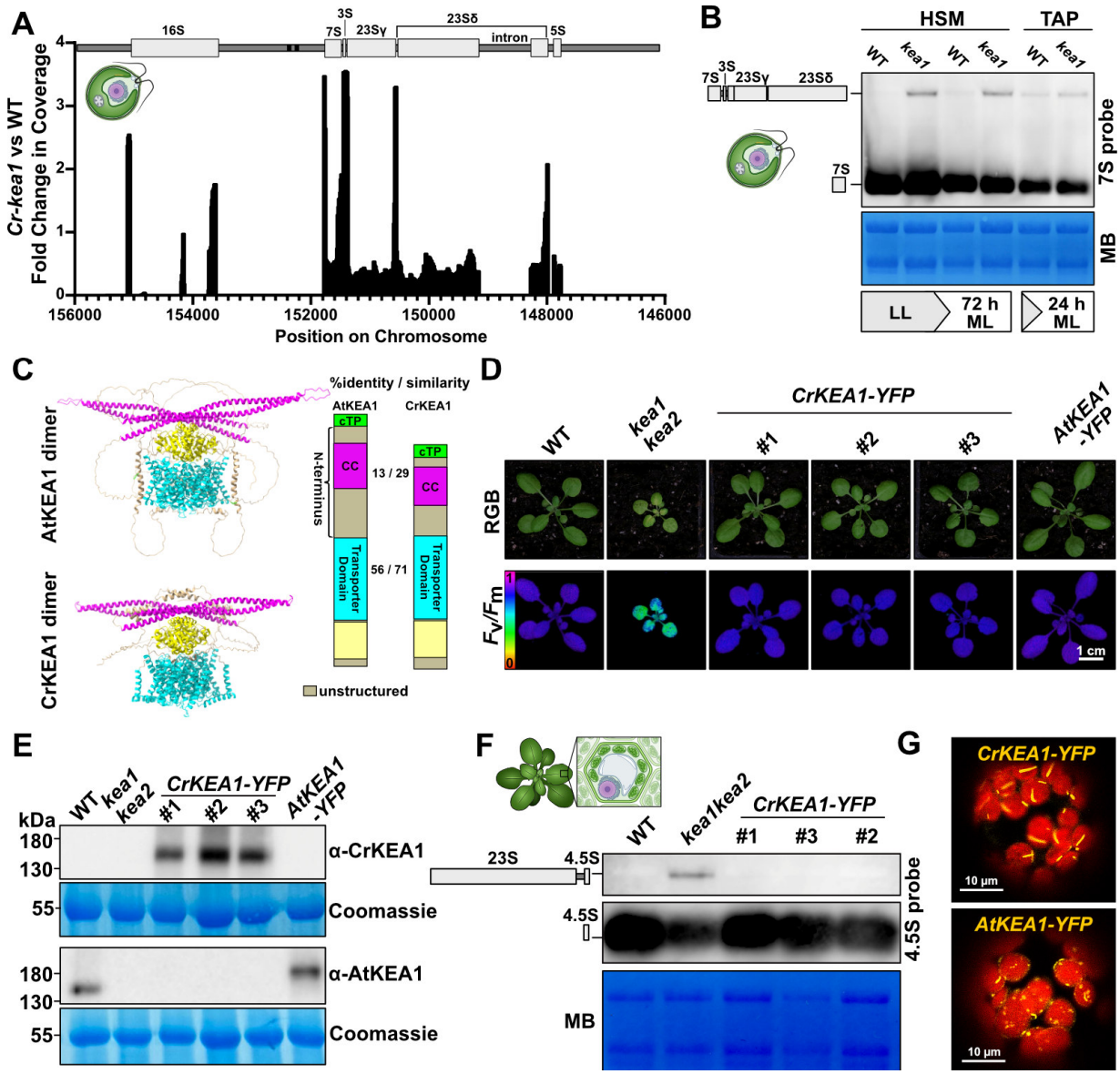


**Figure 6: Conserved role of inner envelope KEA transporters in plastid rRNA processing across algae and higher plants. (A)** Impaired plastid rRNA processing in *kea1* leads to enrichment of the 7S–3S–23S precursor. Shown is the fold change in normalized read coverage (*BamCompare*) from an rRNA-seq experiment comparing *kea1* and WT, revealing increased read density over intergenic regions corresponding to the 7S–3S–23S precursor in the mutant. **(B)** RNA blot analysis using specific plastid rRNA probes confirms accumulation of the 7S–3S–23S precursor in *kea1*. MB, Methylene Blue. **(C)** Structural comparison of AtKEA1 and CrKEA1. AlphaFold3 models of dimeric AtKEA1 and its algal homolog CrKEA1 are shown, with colors corresponding to domain organization depicted to the right. The representation as a dimer was chosen due to the structural findings for the bacterial homolog KefC (Gulati et al., 2024). **(D)** Phenotypical complementation of the Arabidopsis *kea1kea2* mutant by expressing *CrKEA1–YFP*. Scale bar 1 cm. **(E)** Immunoblot validation of *CrKEA1–YFP* expression in complementation lines. **(F)** RNA blot demonstrating restoration of normal plastid rRNA processing in *kea1kea2* upon expression of *CrKEA1–YFP*. MB, Methylene Blue. **(G)** Confocal microscopy of protoplasts isolated from *kea1kea2* plants expressing either *AtKEA1–YFP* or *CrKEA1–YFP*. Chlorophyll autofluorescence (*red*) and YFP signal (*yellow*) displayed in false colors. Scale bar 10 µm.

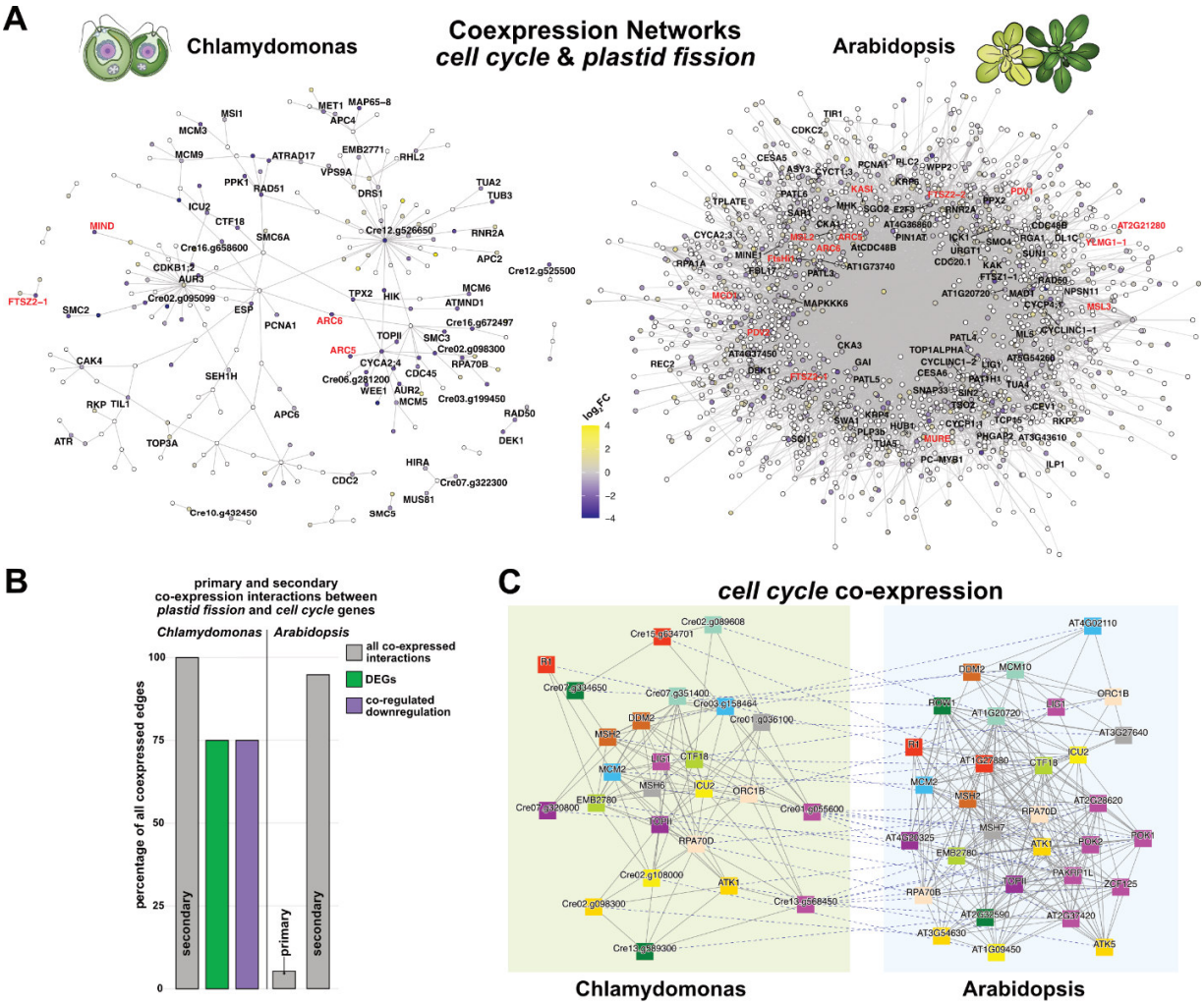


**Figure 7: Comparisons between co-expression networks of Arabidopsis and Chlamydomonas. (A)** From both species, genes annotated to GO:0007049 (*cell cycle*) and GO:0043572 (*plastid fission*) were extracted and visualized based on co-expression relationships in each species. Nodes represent genes and edges connect co-expressed genes. Gene names are black for *cell cycle* and red for *plastid fission*. Nodes represent genes, and edges connect co-expressed genes. White nodes indicate genes that were not significantly changed or not detected; gradient-colored nodes represent DEGs, with color intensity reflecting $\log_2$FC. ML DEGs were used for Chlamydomonas. **(B)** Primary and secondary co-expression interactions between *plastid fission* and *cell cycle* genes found in the networks. Co-regulated downregulation is based on both genes being downregulated DEGs. Cut-off $|\log_2 FC| \geq 0.75$. **(C)** Comparative co-expression network analysis of a *cell cycle* clusters. Nodes represent genes, solid edges connect co-expressed genes and dashed edges connect orthologues. Coloured shapes represent different orthogroups. Cluster comparisons were based on Jaccard Index (JI) computation.

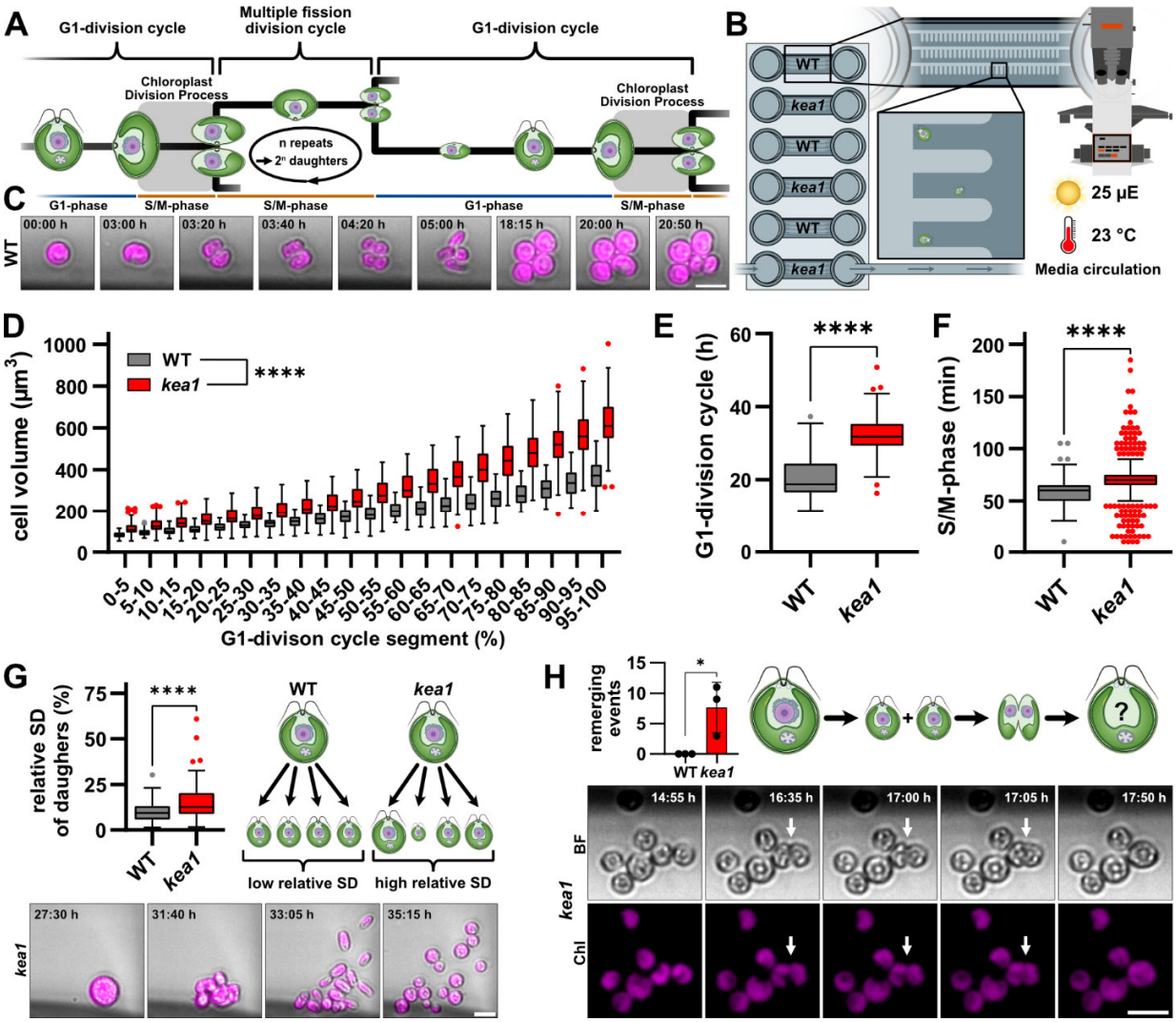


**Figure 8: Single Cell Live Imaging reveals cell cycle defects of *kea1*. (A)** Simplified diagram of the Chlamydomonas cell cycle, showing the labeling of cell-cycle phases used in this study. **(B)** Schematic of the microfluidic flow-cell chip containing hydrogel-based channels with imprinted cavities that immobilize multiple individual cells for long-term observation. 19 WT- and 18 kea1-mother cells including their first generation of G1-daughter cells were analysed. **(C)** Representative time-lapse image series of WT cells illustrating synchronized growth and division. **(D–F)** Quantitative analysis of single-cell trajectories shows that *kea1* cells exhibit significantly increased cell volume in every G1-division cycle segment ($n^{WT}$=67; $n^{kea1}$=90), prolonged G1 phase ($n^{WT}$=68; $n^{kea1}$=90), and extended S/M phase compared to WT ($n^{WT}$=203; $n^{kea1}$=633). **(G)** *kea1* daughter cells display greater size variation following division than WT. Each data point represents the normalized volume difference among daughter cells derived from a single grandmother cell. Daughter cells of $n^{WT}$=55 and $n^{kea1}$=79 grandmothers were compared. **(H)** "Remerging" events, where nearly separated daughter cells fuse again, occur more frequently in *kea1* and were not observed in WT. The bar graph summarizes data from three replicate channels per genotype. *For all panels:* Representative time-lapse series are shown. Scale bars, 10 µm. Box plots follow Tukey's convention. Statistical significance was determined with Mann-Whitney tests (D-G) and unpaired t-test (H) and is indicated by asterisks (* $p < 0.05$; ** $p < 0.01$; *** $p < 0.001$; **** $p < 0.0001$).

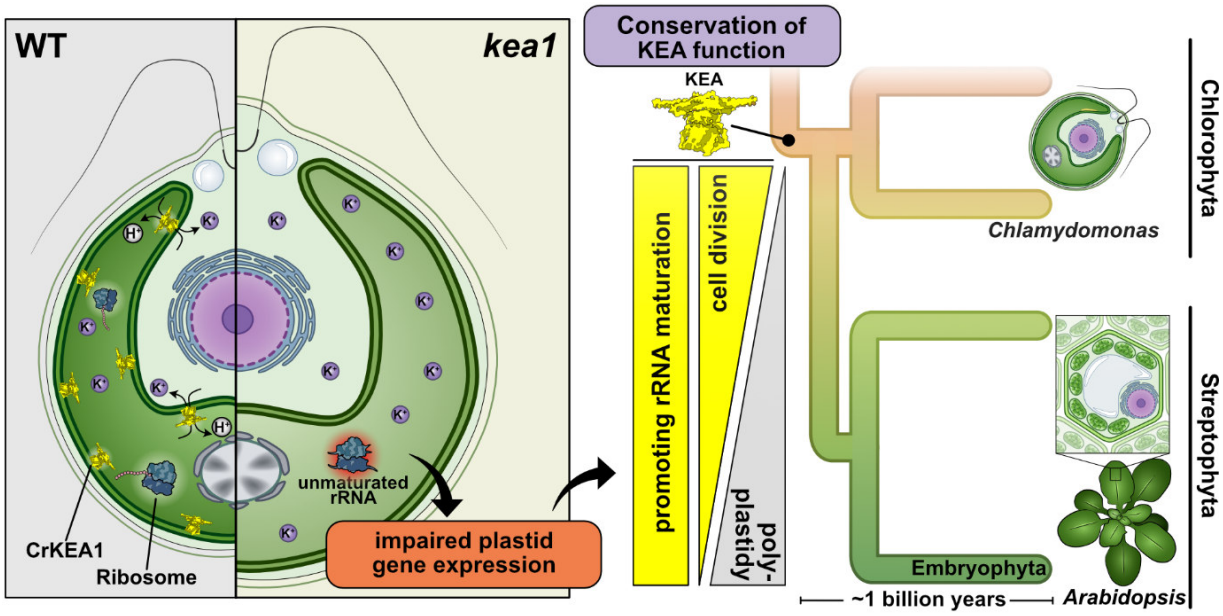


**Figure 9: Working Model: Conserved role of inner envelope KEA transporters across the green lineage.**

In Chlamydomonas, loss of the inner envelope KEA transporters (IE KEAs) leads to $K^+$ imbalance and excess stromal $K^+$, resulting in swollen, misshapen chloroplasts and impaired rRNA processing required for plastid ribosome biogenesis. IE KEAs, including CrKEA1 in Chlamydomonas and AtKEA1/2 in Arabidopsis, are conserved throughout the green branch of the Archaeplastida, spanning the Chlorophyta (green algae) and Streptophyta (charophytes and land plants). All lineages evolved from a monoplastidic unicellular ancestor characterized by tightly coupled plastid and cell division (*monoplastidic bottleneck*, de Vries and Gould, 2018), a condition still retained in Chlamydomonas. During evolution, the emergence of multicellularity and polyplastidy, as in Arabidopsis, relaxed this coupling and allowed plastid division to proceed independently of the cell cycle. Our findings suggest that the importance of IE KEA-mediated ion homeostasis for error-free cell division diminished with the transition to polyplastidy, while its role in maintaining proper rRNA maturation and ribosome assembly remains conserved across Chlorophyta and Streptophyta.

## References


**Abramson J, Adler J, Dunger J, Evans R, Green T, Pritzel A, Ronneberger O, Willmore L, Ballard AJ, Bambrick J, Bodenstein SW, Evans DA, Hung CC, O'Neill M, Reiman D, Tunyasuvunakool K, Wu Z, Žemgulytė A, Arvaniti E, Beattie C, Bertolli O, Bridgland A, Cherepanov A, Congreve M, Cowen-Rivers AI, Cowie A, Figurnov M, Fuchs FB, Gladman H, Jain R, Khan YA, Low CMR, Perlin K, Potapenko A, Savy P, Singh S, Stecula A, Thillaisundaram A, Tong C, Yakneen S, Zhong ED, Zielinski M, Žídek A, Bapst V, Kohli P, Jaderberg M, Hassabis D, Jumper JM** (2024) Accurate structure prediction of biomolecular interactions with AlphaFold 3. Nature **630:** 493-500

**Ahmed T, Yin Z, Bhushan S** (2016) Cryo-EM structure of the large subunit of the spinach chloroplast ribosome. Sci Rep **6:** 35793

**Aihara Y, Fujimura-Kamada K, Yamasaki T, Minagawa J** (2019) Algal photoprotection is regulated by the E3 ligase CUL4-DDB1(DET1). Nat Plants **5:** 34-40

**Aranda-Sicilia MN, Aboukila A, Armbruster U, Cagnac O, Schumann T, Kunz HH, Jahns P, Rodríguez-Rosales MP, Sze H, Venema K** (2016) Envelope K+/H+ Antiporters AtKEA1 and AtKEA2 Function in Plastid Development. Plant Physiol **172:** 441-449

**Baker RT, Catanzariti AM, Karunasekara Y, Soboleva TA, Sharwood R, Whitney S, Board PG** (2005) Using deubiquitylating enzymes as research tools. Methods Enzymol **398:** 540-554

**Bialevich V, Zachleder V, Bišová K** (2022) The Effect of Variable Light Source and Light Intensity on the Growth of Three Algal Species. Cells **11**

**Bierenbroodspot MJ, Darienko T, de Vries S, Delwiche CF, Lorenz M, Ali Z, Irisarri I, Pröschold T, de Vries J** (2025) Phylogenomics unveil a recent origin of morphological complexity in Coleochaetophyceae. Curr Biol **35:** 5071-5080.e5077

**Bisova K, Krylov DM, Umen JG** (2005) Genome-wide annotation and expression profiling of cell cycle regulatory genes in Chlamydomonas reinhardtii. Plant Physiol **137:** 475-491

**Bölter B, Mitterreiter MJ, Schwenkert S, Finkemeier I, Kunz HH** (2020) The topology of plastid inner envelope potassium cation efflux antiporter KEA1 provides new insights into its regulatory features. Photosynth Res **145:** 43-54

**Braun FJ, Hegemann P** (1999) Direct measurement of cytosolic calcium and pH in living Chlamydomonas reinhardtii cells. Eur J Cell Biol **78**: 199-208

**Castandet B, Hotto AM, Strickler SR, Stern DB** (2016) ChloroSeq, an Optimized Chloroplast RNA-Seq Bioinformatic Pipeline, Reveals Remodeling of the Organellar Transcriptome Under Heat Stress. G3 (Bethesda) **6:** 2817-2827

**Catanzariti AM, Soboleva TA, Jans DA, Board PG, Baker RT** (2004) An efficient system for high-level expression and easy purification of authentic recombinant proteins. Protein Sci **13:** 1331-1339

**Catherall E, Musial S, Atkinson N, Walker CE, Mackinder LCM, McCormick AJ** (2025) From algae to plants: understanding pyrenoid-based CO(2)-concentrating mechanisms. Trends Biochem Sci **50:** 33-45

**Chanroj S, Wang G, Venema K, Zhang MW, Delwiche CF, Sze H** (2012) Conserved and diversified gene families of monovalent cation/h(+) antiporters from algae to flowering plants. Front Plant Sci **3:** 25

**Clark-Cotton MR, Chen SA, Gomez A, Mulabagal AJ, Perry A, Malhotra V, Onishi M** (2025) Imaging-based screen identifies novel natural compounds that perturb cell and chloroplast division in Chlamydomonas reinhardtii. Mol Biol Cell **36:** br14

**Clough SJ, Bent AF** (1998) Floral dip: a simplified method for Agrobacterium-mediated transformation of Arabidopsis thaliana. Plant J **16:** 735-743

**Cross FR, Umen JG** (2015) The Chlamydomonas cell cycle. Plant J **82:** 370-392

**Dadras A, Fürst-Jansen JMR, Darienko T, Krone D, Scholz P, Sun S, Herrfurth C, Rieseberg TP, Irisarri I, Steinkamp R, Hansen M, Buschmann H, Valerius O, Braus GH, Hoecker U, Feussner I, Mutwil M, Ischebeck T, de Vries S, Lorenz M, de Vries J** (2023) Environmental gradients reveal stress hubs pre-dating plant terrestrialization. Nat Plants **9:** 1419-1438

**Davies DR, Lyall V** (1973) The assembly of a highly ordered component of the cell wall: The role of heritable factors and of physical structure. Molecular and General Genetics MGG **124:** 21-34

**de Vries J, Gould SB** (2018) The monoplastidic bottleneck in algae and plant evolution. J Cell Sci **131**

**DeTar RA, Barahimipour R, Manavski N, Schwenkert S, Höhner R, Bölter B, Inaba T, Meurer J, Zoschke R, Kunz HH** (2021) Loss of inner-envelope K+/H+ exchangers impairs plastid rRNA maturation and gene expression. Plant Cell **33:** 2479-2505

**DeTar RA, Höhner R, Manavski N, Blackholm M, Meurer J, Kunz HH** (2022) Loss of SALT OVERLY SENSITIVE 1 prevents virescence in chloroplast K+/H+ EFFLUX ANTIPORTER-deficient mutants. Plant Physiol **189:** 1220-1225

**Dogra V, Duan J, Lee KP, Kim C** (2019) Impaired PSII proteostasis triggers a UPR-like response in the var2 mutant of Arabidopsis. J Exp Bot **70:** 3075-3088

**Duanmu D, Casero D, Dent RM, Gallaher S, Yang W, Rockwell NC, Martin SS, Pellegrini M, Niyogi KK, Merchant SS, Grossman AR, Lagarias JC** (2013) Retrograde bilin signaling enables Chlamydomonas greening and phototrophic survival. Proc Natl Acad Sci U S A **110:** 3621-3626

**Dupuis S, Ojeda V, Gallaher SD, Purvine SO, Glaesener AG, Ponce R, Nicora CD, Bloodsworth K, Lipton MS, Niyogi KK, Iwai M, Merchant SS** (2025) Too dim, too bright, and just right: Systems analysis of the Chlamydomonas diurnal program under limiting and excess light. Plant Cell **37**

**Dutcher SK, Li L, Lin H, Meyer L, Giddings TH, Jr., Kwan AL, Lewis BL** (2012) Whole-Genome Sequencing to Identify Mutants and Polymorphisms in Chlamydomonas reinhardtii. G3 (Bethesda) **2:** 15-22

**Emrich-Mills TZ, Yates G, Barrett J, Girr P, Grouneva I, Lau CS, Walker CE, Kwok TK, Davey JW, Johnson MP, Mackinder LCM** (2021) A recombineering pipeline to clone large and complex genes in Chlamydomonas. Plant Cell **33:** 1161-1181

**Fauser F, Vilarrasa-Blasi J, Onishi M, Ramundo S, Patena W, Millican M, Osaki J, Philp C, Nemeth M, Salomé PA, Li X, Wakao S, Kim RG, Kaye Y, Grossman AR, Niyogi KK, Merchant SS, Cutler SR, Walter P, Dinneny JR, Jonikas MC, Jinkerson RE** (2022) Systematic characterization of gene function in the photosynthetic alga Chlamydomonas reinhardtii. Nat Genet **54:** 705-714

**Feeney KA, Hansen LL, Putker M, Olivares-Yañez C, Day J, Eades LJ, Larrondo LF, Hoyle NP, O'Neill JS, van Ooijen G** (2016) Daily magnesium fluxes regulate cellular timekeeping and energy balance. Nature **532:** 375-379

**Gabilly ST, Baker CR, Wakao S, Crisanto T, Guan K, Bi K, Guiet E, Guadagno CR, Niyogi KK** (2019) Regulation of photoprotection gene expression in Chlamydomonas by a putative E3 ubiquitin ligase complex and a homolog of CONSTANS. Proc Natl Acad Sci U S A **116:** 17556-17562

**Galaxy-Community** (2024) The Galaxy platform for accessible, reproducible, and collaborative data analyses: 2024 update. Nucleic Acids Res **52:** W83-w94

**Gallusser B, Weigert M** (2025) TRACKASTRA: Transformer-Based Cell Tracking for Live-Cell Microscopy. *In*. Springer Nature Switzerland, Cham, pp 467-484

**Gorman DS, Levine RP** (1965) Cytochrome f and plastocyanin: their sequence in the photosynthetic electron transport chain of Chlamydomonas reinhardi. Proc Natl Acad Sci U S A **54:** 1665-1669

**Greiner A, Kelterborn S, Evers H, Kreimer G, Sizova I, Hegemann P** (2017) Targeting of Photoreceptor Genes in Chlamydomonas reinhardtii via Zinc-Finger Nucleases and CRISPR/Cas9. Plant Cell **29:** 2498-2518

**Grossman AR, Karpowicz SJ, Heinnickel M, Dewez D, Hamel B, Dent R, Niyogi KK, Johnson X, Alric J, Wollman FA, Li H, Merchant SS** (2010) Phylogenomic analysis of the Chlamydomonas genome unmasks proteins potentially involved in photosynthetic function and regulation. Photosynth Res **106:** 3-17

**Gulati A, Kokane S, Perez-Boerema A, Alleva C, Meier PF, Matsuoka R, Drew D** (2024) Structure and mechanism of the K(+)/H(+) exchanger KefC. Nat Commun **15:** 4751

**Gutman BL, Niyogi KK** (2004) Chlamydomonas and Arabidopsis. A dynamic duo. Plant Physiol **135:** 607-610

**Harris EH, Stern DB, Witman G** (2009) The chlamydomonas sourcebook, Vol 1. Elsevier San Diego, CA

**Henslee EA, Crosby P, Kitcatt SJ, Parry JSW, Bernardini A, Abdallat RG, Braun G, Fatoyinbo HO, Harrison EJ, Edgar RS, Hoettges KF, Reddy AB, Jabr RI, von Schantz M, O'Neill JS, Labeed FH** (2017) Rhythmic potassium transport regulates the circadian clock in human red blood cells. Nat Commun **8:** 1978

**Höhner R, Galvis VC, Strand DD, Völkner C, Krämer M, Messer M, Dinc F, Sjuts I, Bölter B, Kramer DM, Armbruster U, Kunz H-H** (2019) Photosynthesis in Arabidopsis Is Unaffected by the Function of the Vacuolar K+ Channel TPK3. Plant Physiology **180:** 1322-1335

**Holloway SP, Herrin DL** (1998) Processing of a Composite Large Subunit rRNA: Studies with Chlamydomonas Mutants Deficient in Maturation of the 23S-like rRNA. The Plant Cell **10:** 1193-1206

**Holtsmark I, Lee S, Lunde KA, Auestad K, Maple-Grødem J, Møller SG** (2013) Plastid division control: the PDV proteins regulate DRP5B dynamin activity. Plant Mol Biol **82:** 255-266

**Holzner LJ, Östergaard Frank L, Mühlbauer S, Müller A, Schröder L, Seydel C, Grünert J, DeTar RA, Philippar K, Klingl A, Mendoza-Cózatl D, Krämer U, Nägele T, Bölter B, Kunz HH** (2026) The chloroplast ionome shines light on the dynamics of organellar iron homeostasis. Plant Cell **38**

**Honkanen S, Small I** (2022) The GENOMES UNCOUPLED1 protein has an ancient, highly conserved role but not in retrograde signalling. New Phytol **236:** 99-113

1212 **Hotto AM, Castandet B, Gilet L, Higdon A, Condon C, Stern DB** (2015) Arabidopsis
1213 chloroplast mini-ribonuclease III participates in rRNA maturation and intron recycling.
1214 Plant Cell **27:** 724-740
1215 **Julca I, Tan QW, Mutwil M** (2023) Toward kingdom-wide analyses of gene expression. Trends
1216 Plant Sci **28**: 235-249
1217 **Kelterborn S, Boehning F, Sizova I, Baidukova O, Evers H, Hegemann P** (2022) Gene Editing
1218 in Green Alga Chlamydomonas reinhardtii via CRISPR-Cas9 Ribonucleoproteins.
1219 Methods Mol Biol **2379:** 45-65
1220 **Kindle KL** (1990) High-frequency nuclear transformation of Chlamydomonas reinhardtii. Proc
1221 Natl Acad Sci U S A **87:** 1228-1232
1222 **Klein DJ, Moore PB, Steitz TA** (2004) The contribution of metal ions to the structural stability
1223 of the large ribosomal subunit. Rna **10:** 1366-1379
1224 **Knoblauch J, Waadt R, Cousins AB, Kunz HH** (2024) Probing the in situ volumes of
1225 Arabidopsis leaf plastids using three-dimensional confocal and scanning electron
1226 microscopy. Plant J **117:** 332-341
1227 **Kolberg L, Raudvere U, Kuzmin I, Adler P, Vilo J, Peterson H** (2023) g:Profiler-interoperable
1228 web service for functional enrichment analysis and gene identifier mapping (2023 update).
1229 Nucleic Acids Res **51:** W207-w212
1230 **Kunz HH, Armbruster U, Mühlbauer S, de Vries J, Davis GA** (2024) Chloroplast ion
1231 homeostasis - what do we know and where should we go? New Phytol **243:** 543-559
1232 **Kunz HH, Gierth M, Herdean A, Satoh-Cruz M, Kramer DM, Spetea C, Schroeder JI** (2014)
1233 Plastidial transporters KEA1, -2, and -3 are essential for chloroplast osmoregulation,
1234 integrity, and pH regulation in Arabidopsis. Proc Natl Acad Sci U S A **111:** 7480-7485
1235 **Lauersen KJ, Willamme R, Coosemans N, Joris M, Kruse O, Remacle C** (2016) Peroxisomal
1236 microbodies are at the crossroads of acetate assimilation in the green microalga
1237 Chlamydomonas reinhardtii. Algal Research **16:** 266-274
1238 **Li W, Zhang Y, Ren H, Wang Z, OuYang Y, Wang S, Hussain J, Zeb I, Kong Y, Liu S, Qi G**
1239 (2023) Identification of potassium transport proteins in algae and determination of their
1240 role under salt and saline-alkaline stress. Algal Research **69:** 102923
1241 **Li X, Zhang R, Patena W, Gang SS, Blum SR, Ivanova N, Yue R, Robertson JM, Lefebvre**
1242 **PA, Fitz-Gibbon ST, Grossman AR, Jonikas MC** (2016) An Indexed, Mapped Mutant
1243 Library Enables Reverse Genetics Studies of Biological Processes in Chlamydomonas
1244 reinhardtii. Plant Cell **28:** 367-387
1245 **Li Y, Liu D, López-Paz C, Olson BJSC, Umen JG** (2016) A new class of cyclin dependent
1246 kinase in Chlamydomonas is required for coupling cell size to cell division. eLife **5:** e10767
1247 **Lübben MK, Klingl A, Nickelsen J, Ostermeier M** (2024) CLEM, a universal tool for analyzing
1248 structural organization in thylakoid membranes. Physiol Plant **176:** e14417
1249 **Merchant SS, Schmollinger S, Strenkert D, Moseley JL, Blaby-Haas CE** (2020) From
1250 economy to luxury: Copper homeostasis in Chlamydomonas and other algae. Biochim
1251 Biophys Acta Mol Cell Res **1867:** 118822
1252 **Miyagishima SY, Froehlich JE, Osteryoung KW** (2006) PDV1 and PDV2 mediate recruitment
1253 of the dynamin-related protein ARC5 to the plastid division site. Plant Cell **18:** 2517-2530
1254 **Murashige T, Skoog F** (1962) A Revised Medium for Rapid Growth and Bio Assays with
1255 Tobacco Tissue Cultures. Physiologia Plantarum **15:** 473-497
1256 **Neupert J, Karcher D, Bock R** (2009) Generation of Chlamydomonas strains that efficiently
1257 express nuclear transgenes. Plant J **57:** 1140-1150

**Nierhaus KH** (2014) Mg2+, K+, and the ribosome. Journal of bacteriology **196:** 3817-3819

**Niyogi KK** (1999) PHOTOPROTECTION REVISITED: Genetic and Molecular Approaches. Annu Rev Plant Physiol Plant Mol Biol **50:** 333-359

**Okazaki K, Kabeya Y, Suzuki K, Mori T, Ichikawa T, Matsui M, Nakanishi H, Miyagishima SY** (2009) The PLASTID DIVISION1 and 2 components of the chloroplast division machinery determine the rate of chloroplast division in land plant cell differentiation. Plant Cell **21:** 1769-1780

**Pachitariu M, Stringer C** (2022) Cellpose 2.0: how to train your own model. Nat Methods **19:** 1634-1641

**Padovani F, Mairhörmann B, Falter-Braun P, Lengefeld J, Schmoller KM** (2022) Segmentation, tracking and cell cycle analysis of live-cell imaging data with Cell-ACDC. BMC Biol **20:** 174

**Pang X, Nawrocki WJ, Cardol P, Zheng M, Jiang J, Fang Y, Yang W, Croce R, Tian L** (2023) Weak acids produced during anaerobic respiration suppress both photosynthesis and aerobic respiration. Nature Communications **14**: 4207

**Peers G, Truong TB, Ostendorf E, Busch A, Elrad D, Grossman AR, Hippler M, Niyogi KK** (2009) An ancient light-harvesting protein is critical for the regulation of algal photosynthesis. Nature **462**: 518-521

**Perlaza K, Toutkoushian H, Boone M, Lam M, Iwai M, Jonikas MC, Walter P, Ramundo S** (2019) The Mars1 kinase confers photoprotection through signaling in the chloroplast unfolded protein response. Elife **8**

**Peschke M, Moog D, Klingl A, Maier UG, Hempel F** (2013) Evidence for glycoprotein transport into complex plastids. Proc Natl Acad Sci U S A **110:** 10860-10865

**Pettersen EF, Goddard TD, Huang CC, Meng EC, Couch GS, Croll TI, Morris JH, Ferrin TE** (2021) UCSF ChimeraX: Structure visualization for researchers, educators, and developers. Protein Sci **30:** 70-82

**Pootakham W, Gonzalez-Ballester D, Grossman AR** (2010) Identification and regulation of plasma membrane sulfate transporters in Chlamydomonas. Plant Physiol **153:** 1653-1668

**Ramírez F, Ryan DP, Grüning B, Bhardwaj V, Kilpert F, Richter AS, Heyne S, Dündar F, Manke T** (2016) deepTools2: a next generation web server for deep-sequencing data analysis. Nucleic Acids Res **44:** W160-165

**Ramkissoon SH, Mainwaring LA, Sloand EM, Young NS, Kajigaya S** (2006) Nonisotopic detection of microRNA using digoxigenin labeled RNA probes. Mol Cell Probes **20:** 1-4

**Ramundo S, Casero D, Mühlhaus T, Hemme D, Sommer F, Crèvecoeur M, Rahire M, Schroda M, Rusch J, Goodenough U, Pellegrini M, Perez-Perez ME, Crespo JL, Schaad O, Civic N, Rochaix JD** (2014) Conditional Depletion of the Chlamydomonas Chloroplast ClpP Protease Activates Nuclear Genes Involved in Autophagy and Plastid Protein Quality Control. Plant Cell **26:** 2201-2222

**Ramundo S, Rahire M, Schaad O, Rochaix JD** (2013) Repression of essential chloroplast genes reveals new signaling pathways and regulatory feedback loops in chlamydomonas. Plant Cell **25:** 167-186

**Renna L, Papini A, Mancuso S, Brandizzi F, Stefano G** (2025) Plant Plastids: From Evolutionary Origins to Functional Specialization and Organelle Interactions. J Exp Bot

**Reynolds ES** (1963) The use of lead citrate at high pH as an electron-opaque stain in electron microscopy. J Cell Biol **17:** 208-212

**Richter AS, Nägele T, Grimm B, Kaufmann K, Schroda M, Leister D, Kleine T** (2023) Retrograde signaling in plants: A critical review focusing on the GUN pathway and beyond. Plant Commun **4:** 100511

**Rodríguez SG, Crosby P, Hansen LL, Grünewald E, Beale AD, Spangler RK, Rabbitts BM, Partch CL, Stangherlin A, O'Neill JS, van Ooijen G** (2024) Potassium rhythms couple the circadian clock to the cell cycle. bioRxiv

**Rozov A, Khusainov I, El Omari K, Duman R, Mykhaylyk V, Yusupov M, Westhof E, Wagner A, Yusupova G** (2019) Importance of potassium ions for ribosome structure and function revealed by long-wavelength X-ray diffraction. Nature communications **10:** 2519

**Sager R, Zalokar M** (1958) Pigments and photosynthesis in a carotenoid-deficient mutant of Chlamydomonas. Nature **182:** 98-100

**Schmid LM, Manavski N, Chi W, Meurer J** (2024) Chloroplast Ribosome Biogenesis Factors. Plant Cell Physiol **65:** 516-536

**Schmollinger S, Chen S, Strenkert D, Hui C, Ralle M, Merchant SS** (2021) Single-cell visualization and quantification of trace metals in Chlamydomonas lysosome-related organelles. Proc Natl Acad Sci U S A **118**

**Schneider D, Lopez LS, Li M, Crawford JD, Kirchhoff H, Kunz HH** (2019) Fluctuating light experiments and semi-automated plant phenotyping enabled by self-built growth racks and simple upgrades to the IMAGING-PAM. Plant Methods **15:** 156

**Schwartz S, Engstler C, Mühlbauer S, Windenbach E, Wunder T, Kunz HH, Brandt B** (2025) Catch & Release-rapid cost-effective protein purification from plants using a DIY GFP-Trap-protease approach. Plant J **124:** e70544

**Simms D, Cizdziel PE, Chomczyński PA** (1993) TRIzol: A new reagent for optimal single-step isolation of RNA. *In*,

**Small I, Melonek J, Bohne AV, Nickelsen J, Schmitz-Linneweber C** (2023) Plant organellar RNA maturation. Plant Cell **35:** 1727-1751

**Stöberl S, Balles M, Kellerer T, Rädler JO** (2023) Photolithographic microfabrication of hydrogel clefts for cell invasion studies. Lab Chip **23:** 1886-1895

**Strassert JFH, Irisarri I, Williams TA, Burki F** (2021) Author Correction: A molecular timescale for eukaryote evolution with implications for the origin of red algal-derived plastids. Nat Commun **12:** 3574

**Sueoka N** (1960) MITOTIC REPLICATION OF DEOXYRIBONUCLEIC ACID IN CHLAMYDOMONAS REINHARDI. Proc Natl Acad Sci U S A **46:** 83-91

**Sumiya N, Fujiwara T, Era A, Miyagishima SY** (2016) Chloroplast division checkpoint in eukaryotic algae. Proc Natl Acad Sci U S A **113:** E7629-e7638

**Sun L, Ge Y, Sparks JA, Robinson ZT, Cheng X, Wen J, Blancaflor EB** (2019) TDNAscan: A Software to Identify Complete and Truncated T-DNA Insertions. Front Genet **10:** 685

**Supek F, Bošnjak M, Škunca N, Šmuc T** (2011) REVIGO summarizes and visualizes long lists of gene ontology terms. PLoS One **6:** e21800

**Sze H, Chanroj S** (2018) Plant Endomembrane Dynamics: Studies of K(+)/H(+) Antiporters Provide Insights on the Effects of pH and Ion Homeostasis. Plant Physiol **177**: 875-895

**Theis J, Niemeyer J, Schmollinger S, Ries F, Rütgers M, Gupta TK, Sommer F, Muranaka LS, Venn B, Schulz-Raffelt M, Willmund F, Engel BD, Schroda M** (2020) VIPP2 interacts with VIPP1 and HSP22E/F at chloroplast membranes and modulates a retrograde signal for HSP22E/F gene expression. Plant Cell Environ **43:** 1212-1229

1348 **Tulin F, Cross FR** (2014) A microbial avenue to cell cycle control in the plant superkingdom.
1349 Plant Cell **26:** 4019-4038
1350 **Umen JG, Goodenough UW** (2001) Control of cell division by a retinoblastoma protein homolog
1351 in Chlamydomonas. Genes Dev **15:** 1652-1661
1352 **Urrego D, Tomczak AP, Zahed F, Stühmer W, Pardo LA** (2014) Potassium channels in cell
1353 cycle and cell proliferation. Philos Trans R Soc Lond B Biol Sci **369:** 20130094
1354 **Vercruyssen L, Tognetti VB, Gonzalez N, Van Dingenen J, De Milde L, Bielach A, De Rycke**
1355 **R, Van Breusegem F, Inzé D** (2015) GROWTH REGULATING FACTOR5 stimulates
1356 Arabidopsis chloroplast division, photosynthesis, and leaf longevity. Plant Physiol **167:**
1357 817-832
1358 **Vilarrasa-Blasi J, Vellosillo T, Jinkerson RE, Fauser F, Xiang T, Minkoff BB, Wang L,**
1359 **Kniazev K, Guzman M, Osaki J, Barrett-Wilt GA, Sussman MR, Jonikas MC,**
1360 **Dinneny JR** (2024) Multi-omics analysis of green lineage osmotic stress pathways unveils
1361 crucial roles of different cellular compartments. Nat Commun **15:** 5988
1362 **Walther P, Ziegler A** (2002) Freeze substitution of high-pressure frozen samples: the visibility of
1363 biological membranes is improved when the substitution medium contains water. J Microsc
1364 **208:** 3-10
1365 **Wang P, Robert L, Pelletier J, Dang WL, Taddei F, Wright A, Jun S** (2010) Robust growth of
1366 Escherichia coli. Curr Biol **20:** 1099-1103
1367 **Wu FH, Shen SC, Lee LY, Lee SH, Chan MT, Lin CS** (2009) Tape-Arabidopsis Sandwich - a
1368 simpler Arabidopsis protoplast isolation method. Plant Methods **5:** 16
1369 **Wunder T, Brandt B, Kramer L, Kunz H-H** (2025) RNAseq of ribo-depleted RNA from light
1370 treated WT and kea Chlamydomonas. *In*, NCBI Sequence Read Archive (SRA)
1371 **Xu F, Pan J** (2020) Potassium channel KCN11 is required for maintaining cellular osmolarity
1372 during nitrogen starvation to control proper cell physiology and TAG accumulation in
1373 Chlamydomonas reinhardtii. Biotechnol Biofuels **13:** 129
1374 **Zhang Z, Shrager J, Jain M, Chang CW, Vallon O, Grossman AR** (2004) Insights into the
1375 survival of Chlamydomonas reinhardtii during sulfur starvation based on microarray
1376 analysis of gene expression. Eukaryot Cell **3:** 1331-1348

1377